Variable Temperature In Situ Neutron Powder Diffraction and Conductivity Studies of Undoped HoNbO4 and HoTaO4

Bryce Mullens, Matilde Saura-Múzquiz, Giulio Cordaro, Frederick Marlton, Helen Maynard-Casely, Zhaoming Zhang, Gianguido Baldinozzi, Brendan Kennedy

Variable Temperature *In Situ* Neutron Powder Diffraction and Conductivity Studies of Undoped $HoNbO_4$ and $HoTaO_4$

Bryce G. Mullens,[1] Matilde Saura-Múzquiz,[1,2] Giulio Cordaro,[3] Frederick P. Marlton,[1,4] Helen E. Maynard-Casely,[5] Zhaoming Zhang,[5] Gianguido Baldinozzi,[3] and Brendan J. Kennedy[1,*]

[1] School of Chemistry, The University of Sydney, Sydney, New South Wales 2006, Australia

[2] Department of Materials Physics, Faculty of Physics, Universidad Complutense de Madrid, 28040, Madrid, Spain

[3] Université Paris-Saclay, Centralesupélec, Centre National de la Recherche Scientifique (CNRS), Structures, Property and Modeling of Solids (SPMS) Laboratory, 91190 Gif-sur-Yvette, France

[4] Centre for Clean Energy Technology, School of Mathematical and Physical Sciences, Faculty of Science, University of Technology Sydney, Sydney, New South Wales 2007, Australia

[5] Australian Nuclear Science and Technology Organisation, Lucas Heights, New South Wales 2234, Australia

[*] Corresponding Author: Brendan J. Kennedy (brendan.kennedy@sydney.edu.au)

Abstract

Neutron powder diffraction data has been used to quantify the monoclinic (space group $I2/a$) to tetragonal ($I4_1/a$) phase transition that occurs at 775 °C in $HoNbO_4$ and 1300 °C in $HoTaO_4$. In both cases, deviation from second order behavior is evident. The $LnTaO_4$ (Ln = Tb–Er) family of oxides has the potential to adopt one of monoclinic, $I2/a$ or $P2/c$, structures depending on the synthesis conditions. The monoclinic $P2/c$ polymorph of $HoTaO_4$ undergoes an irreversible first order phase transition to the high temperature $I4_1/a$ scheelite-type structure upon heating, with the monoclinic $I2/a$ phase recovered upon cooling. This is the first direct evidence of this irreversible phase transition and implies a maximum heating temperature to synthesize the $P2/c$ phase for potential ionic conductivity applications. Heating a green powder mixture of Ho_2O_3 + Ta_2O_5 revealed a complex series of phase transformations, including the observation of a weberite-type Ho_3TaO_7 intermediate between 1200–1390 °C that was not observed upon cooling. Coupled with electrochemical impedance spectroscopy measurements, this diffraction data provides a structural model that explains the higher mobility of charge carriers in $LnTaO_4$ materials that can be used to identify dopants and improve their ionic conductivity and applicability. Undoped $HoNbO_4$ and $HoTaO_4$ are poor conductors, and the activation energy of tetragonal $HoNbO_4$ is greater than that of the monoclinic polymorph. Oxygen ion and proton conductivities of the undoped structures occur *via* interstitial oxygen sites (~10^{-6} S cm^{-1} at 800 °C), providing a potential avenue to improve their application in practical devices such as solid oxide fuel cells.

ToC Figure

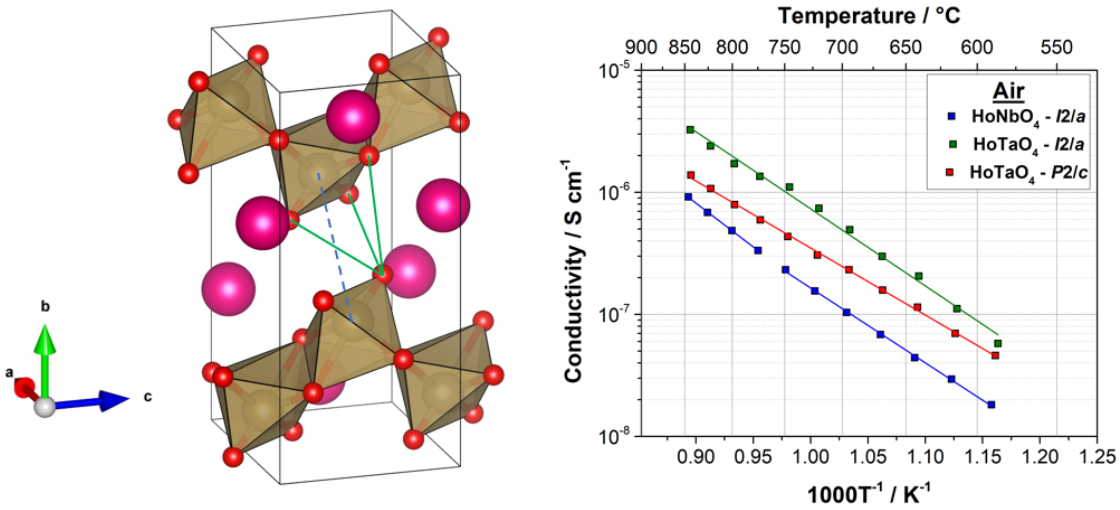

Introduction

The replacement of carbon-emitting energy sources with cleaner alternatives on an industrial scale is a critical priority for limiting the effects of anthropogenic climate change. The global economy needs ways to limit the carbon emissions produced from energy generation and manufacturing processes. One such way is to develop ceramic ionic conductors for use in solid oxide fuel cells (SOFCs) that can potentially produce carbon-neutral energy. SOFCs offer a technological alternative to fossil fuel combustion by facilitating the safe electrochemical oxidation of hydrogen-rich fuels in an all-solid-state environment. Central to the operation of SOFCs is the presence of a material with high ionic conductivity, as well as high thermal and chemical stability in a variety of different chemical environments.[1-3]

One promising avenue for the development of ceramic ionic conductors is the family of ABO_4 materials.[4, 5] These oxide materials have also found applications in photocatalysis,[6, 7] thermal barrier coatings,[8, 9] and as safe storage media for radioactive waste due to their low thermal conductivity and high radiation stability.[10, 11] These oxides are stable in harsh, acidic environments such as carbon dioxide- and hydrogen sulfide-containing fuels commonly used for SOFCs.[3] The crystal structures of ABO_4 materials are largely determined by the relative sizes of the ionic radii, r_A, r_B, and r_O. As described by Bastide, different charge and size combinations of *A* and *B* cations can lead to a wide range of structures.[12] For example, both $CsTcO_4$ and $CsReO_4$ exhibit an orthorhombic *Pnma* structure at room temperature, whereas the corresponding $KTcO_4$ and $KReO_4$ oxides exhibit a tetragonal $I4_1/a$ structure.[13, 14] An additional property of ABO_4 materials, making them appealing SOFC candidates, is the broad range of chemical doping combinations possible within their structure, leading to potential chemical tuning and enhancement of their conductivity properties.

Various ABO_4 materials have been studied intensively for their ionic conductivity. Although purely stoichiometric materials, such as $LaNbO_4$ and $SrWO_4$, display promising properties,[15, 16] small amounts of dopants increase their ionic conductivity by up to three orders of magnitude.[17] $LaNbO_4$ is a promising framework for both oxygen-ion and proton conductivity as the structure can accommodate intrinsic point defects, such as interstitial oxygen ions, that are involved in ion migration.[18-20] The conductivity of these materials can be enhanced by either introducing interstitial oxygen ions through cation doping (such as Mo- or W-doped $LaNbO_{4+\delta}$ displaying high oxygen ion conductivity),[5, 17, 21-23] or by introducing oxygen vacancies (such as Ca-doped $LaNbO_{4-\delta}$ displaying high proton conductivity).[15, 20, 24, 25] Increasing defect concentration enhances conductivity by increasing the amount of charge carriers capable of migrating from one site to another.

Among the ABO_4 structural family, $LnNb_{0.92}W_{0.08}O_{4+\delta}$ compounds (Ln^{3+} = La, Pr, Nd) exhibit large oxygen ion conductivities (up to 3×10^{-3} S cm^{-1} at 800 °C in both dry and wet air).[22] The highest conductivities have been reported for $La_{0.8}Pb_{0.2}WO_4$ (4×10^{-2} S cm^{-1} at 800 °C in air) and $Ca_{0.6}K_{0.4}WO_{3.8}$ (7×10^{-2} S cm^{-1} at 800 °C in air).[26-28] These values are comparable to the ionic conductivity of state-of-the-art electrolytes such as yttria-stabilized zirconia ($Zr_{0.85}Y_{0.15}O_{2-\delta}$, 2×10^{-2} S cm^{-1} at 800 °C in air) and gadolinium-doped ceria ($Ce_{0.9}Gd_{0.1}O_{2-\delta}$, 0.1 S cm^{-1} at 800 °C in air).[1, 2] To date, high proton conductivity has been reported in Ca- and Sr-doped $LaNbO_4$ (~10^{-3} S cm^{-1} for $Ca_{0.01}La_{0.99}NbO_4$ at 950 °C in wet air);[15, 20] about an order of magnitude less than the highest known $BaCeO_3$-based proton conductors (~10^{-2} S cm^{-1} for *Ln*-doped $BaCeO_3$ at 600 °C in wet air). The latter are known to decompose in carbon dioxide-containing atmospheres, limiting their practical use.[29]

There is currently debate in the literature as to whether the lower temperature monoclinic fergusonite-type or the higher temperature tetragonal scheelite-type structure possesses the greater potential for ionic conductivity.[21, 30-32] Work by Bayliss *et al.* suggested that the presence of oxygen ions in the interstitial sites play a significant role, with $CeNbO_{4+\delta}$ recording higher ionic conductivity than its stoichiometric $CeNbO_4$ counterpart.[33] To introduce oxygen ions into interstitial sites, dopant cations (such as substituting Nb^{5+} for W^{6+}) are often added to the structure.[18, 22, 23] However, these substitutions affect the ionic radii ratios proposed by Bastide,[12] altering the behavior and structure of the material at moderate operating SOFC temperatures (500–750 °C).[1] These substitutions can also stabilize the high temperature tetragonal scheelite-type structure at room temperature, circumnavigating the potential first order structural phase transition. At the same time, substitution defects can act as trapping centers, attracting the charge carriers and hampering long-range ion diffusion.[19, 21] Molecular dynamics simulations have confirmed that the total conductivity of these materials is affected by local structural distortions that are common in non-stoichiometric systems.[19, 34, 35] This results in complex relationships between the structural framework of the material and the observed ionic conductivity.

In general, it is desirable to avoid first order structural phase transitions in SOFCs as these could lead to performance issues. Such issues include hysteresis and discontinuities in volume expansion, leading to induced strain and high degradation. This could significantly impinge the use of $LnNbO_4$ materials (Ln^{3+} = lanthanoids La–Lu), as they display a monoclinic-to-tetragonal phase transition within the operating temperature of SOFCs. Early work by Rooksby *et al.* identified that the $ANbO_4$ materials crystallize in the monoclinic system, and undergo a reversible transition to a tetragonal structure before 800 °C.[36] Later, Stubičan identified the monoclinic $I2/a$ to tetragonal $I4_1/a$ phase transition in several $ANbO_4$ orthoniobates to be continuous and reversible ferroelastic phase

transitions, meaning it may not affect the performance of the material as ionic conductors.[37] This was further supported by other studies that observed second order phase transition behavior, as well as its ferroelastic properties.[38-42] However, more recent high-resolution synchrotron X-ray and neutron powder diffraction studies have highlighted the coexistence of both the $I2/a$ and $I4_1/a$ phases at high temperatures, as well as a small thermal hysteresis in the phase transition upon heating and cooling.[43-45] Hysteresis has also been noted in the stress-strain curves observed in single crystal studies of $LaNbO_4$ and $NdNbO_4$.[46] These behaviors are inconsistent with a second order phase transition, suggesting that the $I2/a$ and $I4_1/a$ transition may, in fact, possess first order characteristics that are detrimental to the performance of the material as a component in a ceramic fuel cell.

An additional method of avoiding phase transitions in $Ln NbO_4$-based ionic conductors is to substitute for the analogous $Ln TaO_4$ materials. Whilst Nb^{5+} and Ta^{5+} are described as 'inseparable twins' due to their almost identical ionic radii (0.64 Å in octahedral coordination),[47] several differences have been observed in their crystal chemistry, particularly in ABO_4-type structures.[25, 48] Whilst the lanthanoid orthoniobates ($Ln NbO_4$) are invariably reported to crystallize in the $I2/a$ structure, the lanthanoid orthotantalates ($Ln TaO_4$) possess more structural flexibility, crystallizing in the monoclinic space groups $P2_1/c$, $I2/a$ (termed "M-type"), or $P2/c$ (termed "M'-type") (see Figure 1).[49] A recent study by Mullens *et al.* also observed the synthesis of $Ln TaO_4$ (Ln = Tb–Ho) was sensitive to the thermal history of the material, with lower temperatures favoring the $P2/c$ structure and higher temperatures favoring $I2/a$.[49] In addition to their crystal chemistry, $Ln TaO_4$ materials have shown different behavior at elevated temperatures. The $I2/a$ to $I4_1/a$ phase transition has been reported in several $LnBO_4$ (B = Nb, Ta) compounds and is dependent on the size of the Ln^{3+} cation ($LaNbO_4$ T_c = ~480 °C, $HoNbO_4$ T_c = ~810 °C) and on the choice of B-site cation ($NdNbO_4$ T_c = ~660 °C, $NdTaO_4$ T_c = ~1220 °C).[37, 44, 50] The chemical tunability of both the A and B sites of the ABO_4 material presents an opportunity to specifically tailor these materials for ionic conductivity by altering the temperature of its first order phase transition, moving it outside of the operating temperature of SOFCs. Although this has been extensively studied in $Ln NbO_4$ materials, the analogous $Ln TaO_4$ structures present an untapped potential to explore the effects of ionic conductivity in relation to their different room-temperature polymorphs, phase transitions, and high stability at elevated temperatures.

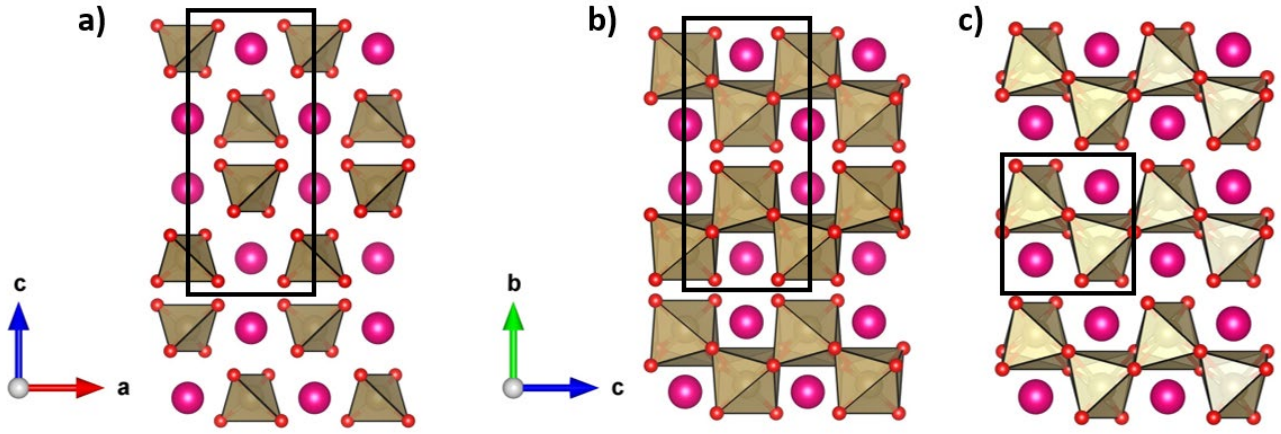

Figure 1: Representations of the *Ln*TaO_4 structures, with (a) the tetragonal scheelite $I4_1/a$, (b) the monoclinic fergusonite $I2/a$ (*M*-type), and (c) the monoclinic $P2/c$ (*M*'-type). The unit cell of each structure is indicated with a black box. In each case, the *Ln* cations are shown as pink spheres, the Ta polyhedra are shown in brown, and the oxygen anions are shown as red spheres.

There is often a disjoint between conductivity studies of metal oxides that are, by necessity, conducted at high temperatures and structural studies that are typically measured either under ambient conditions or using less sensitive X-ray methods. This work seeks to address this disconnect through a comprehensive variable temperature neutron diffraction study of the monoclinic $P2/c$ and $I2/a$ phases observed in the *Ln*TaO_4 series, supplemented by electrochemical impedance spectroscopy measurements. Our goal was to relate the $I2/a$ and $P2/c$ structures with the ionic and electronic conductivities in undoped *LnB*O_4 materials in order to provide tools for the identification of compositions suitable for doping. This study first describes the variable temperature structural behavior of $HoNbO_4$ and $HoTaO_4$ using neutron powder diffraction (NPD), filling a previous gap in the literature by determining the nature of the irreversible $P2/c$ to $I4_1/a$ phase transition. A variable temperature NPD experiment was then carried out on a stoichiometric mix of Ho_2O_3 + Ta_2O_5 green powder to determine the optimal synthesis conditions of either the $I2/a$ or $P2/c$ phases of $HoTaO_4$ using a solid-state reaction. Finally, in light of the NPD studies, the ionic conductivity of the undoped $I2/a$ and $P2/c$ phases of $HoTaO_4$ were compared to that of $HoNbO_4$, which possesses a phase transition within the operating temperature of SOFCs.

Experimental Section

Samples with the composition HoBO$_4$ (B^{5+} = Nb, Ta) were prepared using a conventional solid state synthesis route. The metal oxides Ho_2O_3 (Aithaca Chemicals, 99.999%), Nb_2O_5 (Aithaca Chemicals, 99.99%), and Ta_2O_5 (Aithaca Chemicals, 99.99%) were dried at 1000 °C for 15 hours to remove adsorbed water and carbon dioxide. Stoichiometric amounts of the starting reagents, sufficient to prepare 5 g of each sample, were weighed and mixed in acetone until a slurry was formed. The slurry was finely mixed by hand in an agate mortar before the dried powder was placed into an alumina crucible and heated to 1000 °C for 24 hours. After hand mixing again, the samples were pressed into rods using a hydrostatic press at 200 bar for 10 minutes. The rods were then heated in air at 1200 °C for 24 hours and 1400 °C for 48 hours, with intermittent grinding and repressing. To synthesize $HoTaO_4$ in the $I2/a$ space group for ionic conductivity measurements, a sample of $HoTaO_4$ (in the $P2/c$ space group, prepared by heating to 1400 °C) was pressed into a rod and heated in air at 1450 °C for a further 24 hours. As an additional experiment, a green powder of Ho_2O_3 + Ta_2O_5 was prepared by milling with ethanol (1 g:1 mL mixture) in a planetary ball mill at 250 rpm for 1 hour before being thoroughly reground in an agate mortar and pestle. The compositions were confirmed by X-ray fluorescence; see Tables S1-3 of the supplementary information.

NPD experiments were performed with neutrons of wavelength 1.541(1) Å, obtained with a Ge [335] monochromator on Wombat, the high intensity neutron diffractometer at the Open Pool Australian Lightwater (OPAL) reactor.[51] Single phase polycrystalline samples of $HoNbO_4$ and $HoTaO_4$ were pressed into rods and sintered at 1000 °C in air for 24 hours before diffraction measurements to remove any absorbed water or carbon dioxide. Each sample was then cooled at 5 ° min^{-1}. The mixed oxide green powder was pressed into a rod but was not preheated to avoid any potential reaction. The sample of $HoNbO_4$ was loaded into a 6 mm diameter vanadium can and affixed to a sample stick made of tantalum. The $HoTaO_4$ and Ho_2O_3 + Ta_2O_5 green powder samples were loaded into 6 mm diameter open niobium cans, with the top of the can covered with a niobium wire mesh. Each sample was formed into a rod using a hydrostatic press to ensure minimal reaction or cation exchange between the samples and the Nb can. For each measurement, the whole assembly was placed in an ILL-type high-vacuum furnace fitted with Nb heating elements and operated at $<10^{-4}$ Pa during the measurements. The temperature was measured using a thermocouple positioned within the sample stick, adjacent to where the samples were affixed. Variable temperature NPD data were collected on both heating and cooling of the samples. There was no significant change in the background of the NPD patterns throughout the measurements, indicating there was little, if any, hydrogen-containing species such as water lost during the measurements. Data were collected for

periods of four minutes. More details on the heating and cooling rates are given in the supporting information (SI).

The structures were refined using the Rietveld method as implemented in TOPAS6.[52] The peak shapes were modelled using the Thompson-Cox-Hastings profile parameters,[53] and the background was estimated using a 6th-order Chebyshev function. An additional peak was observed across all datasets at ~37 ° 2θ due to the Nb heating elements of the furnace, which was modelled using an extra pseudo-Voigt background peak. Reflections from the Nb can were modelled using the Le Bail fitting method. The space groups of each material were established by considering the cell metric and systematic absences. The background, scale factor, detector zero-point, lattice parameters, atomic coordinates, and isotropic atomic displacement parameters (ADPs) were refined together with the peak profile parameters. The Rietveld refinements were then performed sequentially, with the structure updated after each refinement. The sequential refinements were undertaken starting from both the low temperature monoclinic region and the high temperature tetragonal region, for data measured on both heating and cooling. The crystal structures were drawn using VESTA.[54]

For the conductivity measurements, the samples were pressed into pellets at 5 MPa for 15 minutes using an isostatic press. These were then sintered in air at 1550 °C ($HoNbO_4$ and $HoTaO_4$ *I*2/*a*) or 1350 °C ($HoTaO_4$ *P*2/*c*) before being cooled to room temperature at a rate of 3 ° min^{-1}. Two or more pellets of each sample were obtained with 1.0–1.5 mm thickness and sufficient relative density for the electrochemical measurements. The experimental density of each sample was obtained using electronic calipers for the geometrical parameters of the pellets and a high precision electronic balance for the mass. The relative density was calculated as the ratio of the experimental density and the theoretical density of the sample obtained from previous synchrotron X-ray diffraction measurements.[49, 55] The relative densities are reported in the SI (Table S4). Before each measurement, pellets were coated in a conductive Pt paste and reheated to 1000 °C for two hours to cure the paste.

Samples were mounted into a Probostat^{TM} setup using a spring system to ensure good contact with two Pt grids acting as both current collectors and gas distributors. A calibrated thermocouple was placed immediately next to the sample, and the reported temperatures were the measured values, rather than the experimental setpoints. A gas flow rate of 1 L hr^{-1} was selected for the measurements in air (80% N_2, 20% O_2. pH_2O <0.1%. Air Liquide), Ar (Air Liquide), wet Ar, and wet 5% H_2 in Ar (Air Liquide), with the gas prewarmed before entering the sample space. The wet atmosphere was obtained by flowing the gases through a water bubbler at room temperature (*i.e.,* 2.3% water partial pressure, 100% relative humidity at 20 °C). The setup was inserted into a vertical furnace to perform

electrochemical impedance spectroscopy (EIS) measurements between 850–600 °C at 25 °C intervals while cooling. A minimum temperature of 600 °C was selected as the impedance in Ar, below this threshold exceeded the equipment entry resistance (~2×10^7 Ω), leading to unreliable results. Impedance spectra were recorded in the 10^6–0.1 Hz frequency range using a Solartron 1260 model potentiostat with an AC amplitude of 100 mV. The EIS spectra were fitted in ZView®, and the obtained resistance values were normalized over the pellet thickness and the active surface area to calculate the conductivity in S cm^{-1}.

Results and Discussion

(i) *In Situ Neutron Diffraction Measurements of $HoNbO_4$: Observation of the Reversible I2/a to $I4_1/a$ Phase Transition*

The structures of $HoNbO_4$ at 50 and 1000 °C were established using Rietveld refinement against the NPD datasets (see Figure 2, Table S5). The fergusonite model in the monoclinic *I*2/*a* space group was successfully fit to the 50 °C data, consistent with previous studies.[55, 56] In this monoclinic structure, the Nb cations are surrounded by four close oxygen ions, two O(1) and two O(2) with Nb–O bond distances of 1.847(4) Å and 1.930(4) Å respectively, as well as two additional O(2') ions with Nb–O bond distances of 2.437(4) Å. Bond valence sums (BVS) were calculated for the Nb^{5+} cation coordinated as both tetrahedra (NbO_4) and octahedra (NbO_6) to determine the optimal coordination environment. The BVS, S_{ij}, was calculated by considering the valences of the individual bonds using

$$S_{ij} = \sum \exp\left[\frac{R_0 - R_{ij}}{b} \right]$$

where R_0 is a tabulated parameter of the 'ideal' bond length, R_{ij} is the observed bond length, and b is an empirical constant equal to 0.37.[57, 58] Including the two long O(2') contacts in the Bond Valence Sum (BVS) calculations increased the Nb^{5+} BVS from 4.29 to 4.77 meaning the Nb^{5+} sites are best described as heavily distorted NbO_6 octahedra.[57] Previous computational studies have also highlighted the importance of these additional long *B*–O contacts.[55]

The tetragonal scheelite $I4_1/a$ model was successfully refined to the diffraction pattern measured at 1000 °C. The Nb cations are surrounded by four close oxygen ions with identical Nb–O bond distances of 1.888(3) Å. However, due to the slight difference in Nb-O bond angles (O–Nb–O = 105.9 and 116.9 °), it is appropriate to describe NbO_4 as distorted tetrahedra. The BVS of NbO_4 is 4.26, meaning Nb^{5+} is significantly underbonded. It has been hypothesized from previous density functional theory (DFT) studies and maximum entropy method (MEM) analysis that this may facilitate the occupancy of nearby interstitial sites, enhancing oxygen ion conductivity.[26, 35] [21, 59]

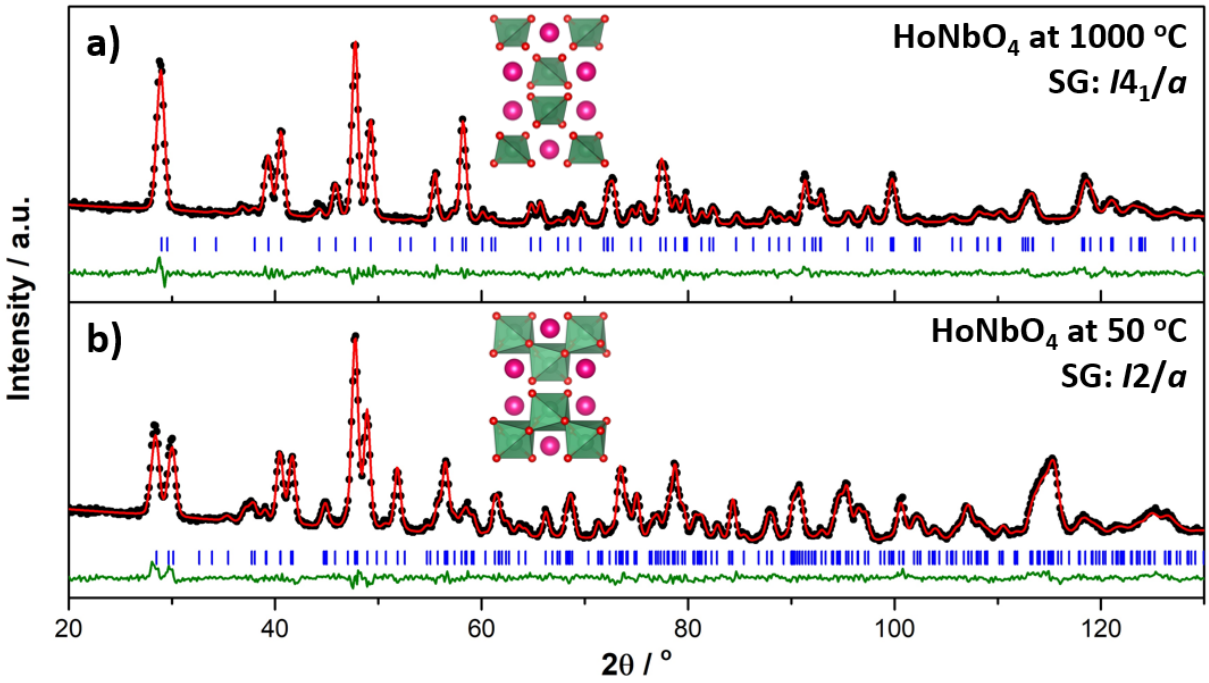

Figure 2: Rietveld refinement results for neutron powder diffraction data of $HoNbO_4$, measured at 1.541(1) Å. Below 775 °C, the structures were refined using a monoclinic *I*2/*a* model and above 775 °C, the structures were refined using a tetragonal $I4_1/a$ model. In both cases, the black circles represent the observed data, the solid red line represents the fit to the measured data, and the lower green line represents the difference between the observed and calculated data. The blue vertical tick marks show the positions of the space group allowed Bragg reflections.

The temperature dependence of the NPD patterns and the refined lattice parameters for $HoNbO_4$ are shown in Figures 3-4 (and in Figures S2–4). Upon heating, the monoclinic cell undergoes anisotropic expansion, with the monoclinic *a* parameter decreasing whilst the *c* parameter increases. A phase transition is observed at approximately 775 °C where the *a* and *c* lattice parameters become equal, indicating an increase in symmetry (Figure 4a). That the background in the NPD patterns did not significantly change during heating demonstrates there were no hydrogen species such as water present in the sample, recalling that hydrogen is a large incoherent neutron scatterer which increases the background of the diffraction patterns. This is consistent with the lack of any apparent discontinuities in the lattice parameters or unit cell volume upon heating that would accompany the loss of intercalated water; a conclusion further supported by *ex situ* thermogravimetric analysis (Figure S1). The unit cell volume also increases linearly in both the monoclinic and tetragonal phases, with a small change in the expansion rate at the phase transition (Figure 4b). This is accompanied by a decrease in the monoclinic β angle approaching 90 °, as expected for a monoclinic *I*2/*a* to tetragonal $I4_1/a$ phase transition (Figure 4c). Similar behavior was observed in a recent study of the *I*2/*a* to $I4_1/a$

phase transition in $NdNbO_4$.[44] The *y* atomic coordinates of Ho^{3+} and Nb^{5+} also change upon heating, with the cations moving from the general (1/4, *y*, 0) and (1/4, *y*', 0) positions in the monoclinic structure to the symmetrically-constrained (0, 1/4, 5/8) and (0, 1/4, 1/8) positions in the tetragonal structure (Figure S3). Plotting the monoclinic β angle against the *y* positional parameter of the Nb^{5+} cation reveals a linear relationship, demonstrating a strong coupling between the atomic structure and the unit cell parameters (Figure S4).

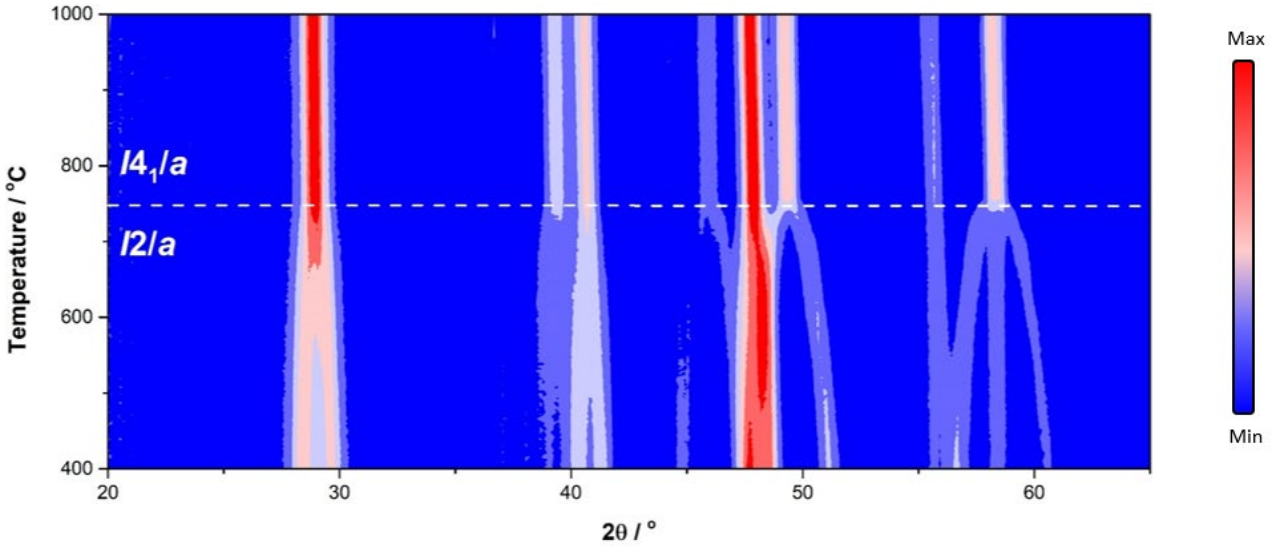

Figure 3: Portions of the temperature dependent neutron powder diffraction patterns for $HoNbO_4$ measured on heating to 1000 °C. The *I*2/*a* to *I*4$_1$/*a* phase transition temperature is indicated by the dashed line. The data were collected at 1.541(1) Å.

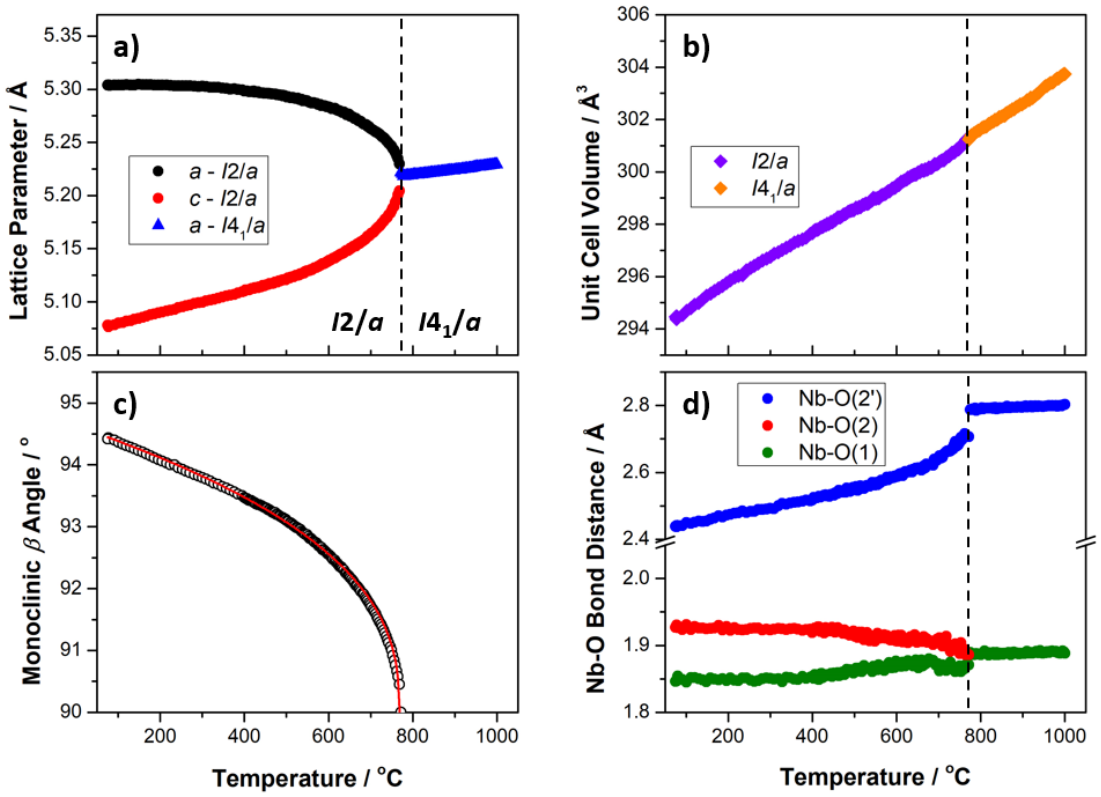

Figure 4: Temperature dependence of the unit cell parameters for $HoNbO_4$ obtained by Rietveld refinements against neutron powder diffraction data. The data were collected as the sample was heated from room temperature to 1000 °C. The error bars are smaller than the symbols. The solid line in © is a fit described in the text.

The nature of the monoclinic *I*2/*a* to tetragonal *I*4$_1$/*a* phase transition in *AB*O_4 oxides has been discussed previously, with earlier studies suggesting that the phase transition was purely ferroelastic in nature.[38-41] However, Arulnesan *et al*. concluded that the phase transition was first order due to the breaking of the longer Nb–O(2') bonds upon heating.[43] This conclusion was supported in recent studies by Saura-Múzquiz *et al.* and Auckett *et al.* that identified the Γ_2^+ mode as a primary order parameter responsible for the change in bonding of the NbO_6 polyhedra.[21, 44] This is also observed in the current study of $HoNbO_4$ (Figure 4d), with a 'breaking' of the longer Nb–O(2') occurring across the phase transition. More details of the nature of the *I*2/*a* to *I*4$_1$/*a* phase transition are outlined below.

In the present work, the possibility of a first order phase transition was investigated by attempting to fit a two-phase model between the temperatures of 750–778 °C. The coexistence of the monoclinic and tetragonal phases has been observed in several recent high resolution diffraction studies of related *A*NbO_4 systems.[43, 45, 60] First order phase transitions are characterized by a sudden change in the thermodynamic properties of the material, meaning it is possible (but not required) for the two phases to coexist around the transition temperature. Initially, the patterns at 750 and 778 °C were plotted

against each other to determine any regions of interest indicative of the monoclinic-to-tetragonal phase transition. At 2θ ~45 °, four reflections associated with the $I2/a$ phase merge to become a single (213) reflection in the $I4_1/a$ phase. Similarly, at 2θ ~49 °, three reflections associated with the $I2/a$ phase merge to become a single (220) reflection in the $I4_1/a$ phase. In these ranges, there was no indication of a coexistence of the sets of reflections, indicating the absence of a two-phase region. This was further investigated by plotting the R_{wp} values across this temperature range. The values appear to vary systematically across the transition, indicating that the refinement does not require the inclusion of an additional phase to accurately model the data (Figure S5). The transition was also investigated by differential scanning calorimetry (DSC); however, no transition enthalpy was observed (Figure S1), consistent with other similar compounds that display the same phase transition.[61, 62] That no two-phase region is observed upon heating or cooling, or the absence of a transition enthalpy spike in the DSC, suggests that the transition may be continuous (either second order or tricritical) and reversible.

The nature of the phase transition in the present oxides was further investigated using the framework of Landau mean-field theory. The $I2/a$ to $I4_1/a$ phase transition has been described as purely ferroelastic in previous Raman spectroscopy studies.[38, 63, 64] The existence of a soft acoustic mode belonging to the B_g irreducible representation was identified by Gu *et al.* using Brillouin scattering. This is the primary order parameter of the phase transition and corresponds to both the $(\epsilon_1 - \epsilon_2)$ and ϵ_6 strain components.[65] In this case, Landau mean-field theory was used to set up a series expansion of the Gibbs free energy difference between the low temperature monoclinic $I2/a$ and high temperature tetragonal $I4_1/a$ phases. A full derivation is found in the SI and summarized in Table S6. The Gibbs free energy difference consists of three contributions: G_ϵ from the ferroelastic order parameters describing the strains of B_g symmetry, G_η describing the atomic displacements of B_g symmetry, and G_c describing the coupling between the two.

Previous work by Wada *et al.* suggested the ϵ_6 strain component to be the primary order parameter, with η denoting the amplitude of the order parameter describing atomic displacements produced by the optic phonon of B_g symmetry.[66] The symmetrized elastic contribution may be approximated as

$$G_\epsilon(\epsilon_6) = \frac{A}{2}(T - T_c)\epsilon_6^2 + \frac{B}{4}\epsilon_6^4$$

where A and B are constant (positive) coefficients. As there are only two potential phases, the expansion is limited to the fourth order with respect to ϵ_6. If the phase transition is driven by this strain component, the B coefficient may be taken as sufficiently small (relative to A) such that it may be neglected. This leads to a proportionality of $\epsilon_6 \propto (T - T_c)^\beta$, where β is the critical exponent, and

may be taken as 0.5 for second order behavior. The coupling term in the Gibbs free energy difference expansion, G_c, accounts for the interactions between the acoustic and optic modes of B_g symmetry. This is given as

$$G_c(\epsilon_6, \eta) = -c_1\epsilon_6(\epsilon_1 - \epsilon_2) - c_2\epsilon_6\eta - c_3\epsilon_6^2(\epsilon_1 + \epsilon_2 + \epsilon_3)$$

where c_1, c_2, and c_3 are constants, and the $(\epsilon_1 + \epsilon_2 + \epsilon_3)$ term is the volume variation.

The effect of the coupling term means there are several possible choices for the order parameter. As a consequence of the medium peak-shape resolution of the neutron diffractometer and previous studies, the ϵ_6 strain component was analyzed due to the accuracy of the structural data and its linear coupling to the order parameter (Figure 5a). Fits to other parameters, such as the Nb(y) atomic coordinate, the $(\epsilon_1 - \epsilon_2)$ strain parameter, and the monoclinic β angle are found in the SI (Figures S6–8).

Initially, it was attempted to fit the temperature dependence of the ϵ_6 strain parameter over the entire measured temperature range with a critical exponent $\beta = 0.5$. This resulted in poor fits, however least-squares fitting to the general expression $\eta \propto \epsilon_6 = A(T_c - T)^{\beta}$ provided an acceptable fit with $\beta = 0.441$ and $T_c = 772$ °C (Figure 5a). This value is similar to that reported in previous studies, with Sarin *et al.* reporting $0.350 \leq \beta \leq 0.405$ for other ANbO$_4$ oxides (A = La, Dy, Y) and with $\beta = 0.398$ reported by Saura-Múzquiz *et al.* for NdNbO$_4$, although it should be noted that these studies treated the monoclinic β angle as the primary order parameter. Fits to the monoclinic β angle returned a critical exponent $\beta = 0.390$ and $T_c = 768$ °C (Figure S8a).[44, 45] If the fitting temperature range is reduced to within ~50 °C of the phase transition, a fit of $\beta = 0.5$ with 774 °C is achieved, implying Landau mean-field theory-type behavior close to the phase transition, and a departure from mean-field behavior far from T_c (Figure 5b).

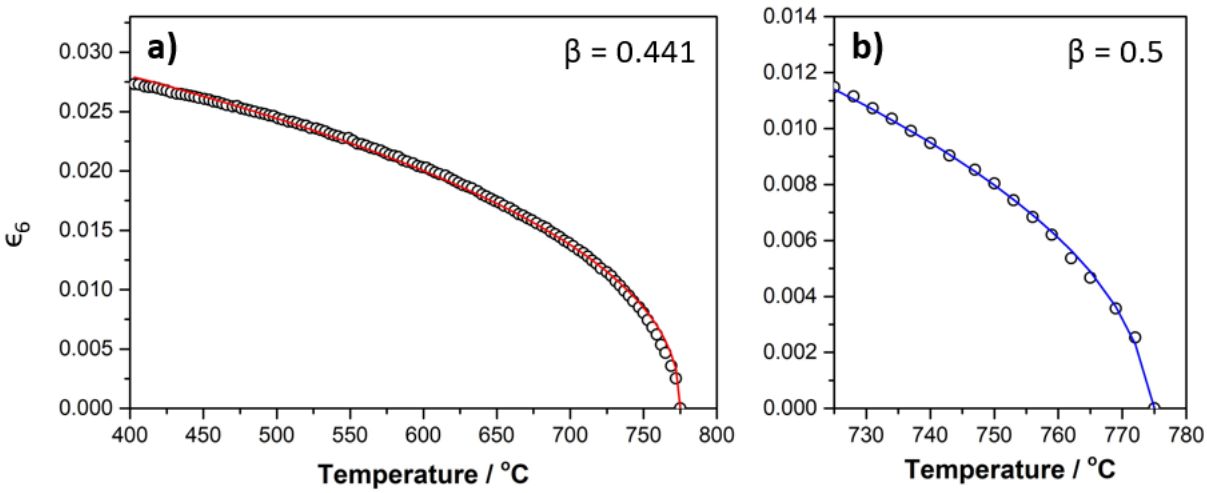

Figure 5: Fits to the ϵ_6 strain parameter of $HoNbO_4$ variable temperature data using the power law as described in the text, (a) fitted over the entire measured temperature range, and (b) fitted within 50 °C of the phase transition temperature. Although the fit was performed over the entire temperature range, the plots show from 400–800 °C for clarity.

As the critical exponent $\beta \neq 0.5$ when fitting across the entire temperature range, it is evident that Landau mean-field theory does not capture the full nature of the phase transition, suggesting more complex behavior far from T_c. It is thought that coupling between the second order ferroelastic displacements of the NbO_6 groups and the first order breaking of the long Nb–O(2') bond occurs. Upon cooling, no two-phase region was observed between the tetragonal $I4_1/a$ and monoclinic $I2/a$ phases. However, a small hysteresis was observed, with T_c = 768 °C upon heating and T_c = 761 °C upon cooling. This suggests a small discontinuity in the enthalpy of the phase transition that was not apparent in the DSC. The Landau analysis indicates that the transition is not strictly second order, noting that bond breaking is a first order process.

(ii) In Situ Neutron Diffraction Measurements of $HoTaO_4$: Observation of the Irreversible P2/c to $I4_1/a$ Phase Transition

The structures of $HoTaO_4$ at 50, 1500, and 50 °C upon cooling were established by Rietveld refinements against the NPD data (Figure S9, Table S7). The monoclinic *P*2/*c* structure was successfully refined to the room temperature data consistent with previous studies.[55, 67] Refinements where the oxygen vacancies were allowed to vary showed no evidence for either measurable oxygen non-stoichiometry, nor occupancy of interstitial sites. Furthermore, the atomic displacement parameters, that correlate with oxygen vacancies for the anion sites, were unremarkable. It should be noted it is unexpected for $HoNbO_4$ and $HoTaO_4$ to crystallize into different space groups, given the similar Shannon ionic radii of Nb^{5+} and Ta^{5+}.[47] Similar to the *I*2/*a* monoclinic structure observed for $HoNbO_4$, the Ta^{5+} cations are surrounded by four close oxygen ions, two O(1) at 1.882(5) Å and two O(2) at 2.015(5) Å, giving an average Ta–O bond length of 1.949(2) Å. However, there are two additional O(2') ions with Ta–O bond distances of 2.222(5) Å. These are much closer than the additional O(2') bonds seen in $HoNbO_4$. Inclusion of these additional contacts raises the BVS from 3.80 for TaO_4 to 4.72 for TaO_6, which indicates a better model of its coordination environment.[57] Previous DFT studies have identified the importance of these longer Ta–O(2') contacts, with significant covalent character observed due to the radial extension of the Ta(5*d*) orbitals.[55]

The tetragonal scheelite-type $I4_1/a$ structure was successfully refined against the diffraction pattern measured at 1500 °C, as observed above for $HoNbO_4$ at 1000 °C. In the tetragonal structure, the Ta^{5+} cations are surrounded by four close oxygen ions with identical Ta–O bond distances of 1.918(4) Å, with a similar distortion in bond angles (O–Ta–O = 105.9 and 116.8 °). The BVS of TaO_4 is 4.72, meaning that Ta^{5+} is slightly underbonded, as was observed for the corresponding $HoNbO_4$ structure.

Upon cooling, $HoTaO_4$ crystallizes into a different space group, and the reflections indicative of the primitive monoclinic cell were absent (Figure S10). The monoclinic *I*2/*a* fergusonite-type model was successfully refined against the NPD data (Table S7). Therefore, it appears that heating $HoTaO_4$ from *P*2/*c* through the high temperature $I4_1/a$ phase causes it to recrystallize in the *I*2/*a* phase that is isostructural to that seen for $HoNbO_4$. This is the first *in situ* analysis of this phase transformation. Comparing isostructural $HoNbO_4$ and $HoTaO_4$ at similar temperatures reveals these have comparable bond lengths with similar atomic coordinates. The same phenomenon has been previously observed, where the *B*–O(2') long bond is shorter in TaO_6 than the corresponding NbO_6 polyhedra (Table 1).[44, 49, 55]

Table 1: Comparison of the NbO_6 and TaO_6 polyhedra environments in isostructural, *I*2/*a*, $HoNbO_4$ (upon heating) and $HoTaO_4$ (upon cooling) at 120 °C.

	$HoNbO_4$ (SG *I*2/*a*)	**$HoTaO_4$ (SG *I*2/*a*)**
***B*-O(1) (Å)**	1.847(4)	1.845(7)
***B*-O(2) (Å)**	1.930(4)	1.955(7)
***B*-O(2') (Å)**	2.437(4)	2.362(7)
***B*-O Average (Å)**	2.0715(17)	2.0539(19)
***B*O$_6$ Volume (Å^3)**	10.35	10.33
***B*O$_6$ BVS**	4.77	4.88

The temperature dependence of the appropriately scaled lattice parameters is shown (Figure 6). Upon heating, the *P*2/*c* phase undergoes expansion in all three lattice directions. This is accompanied by a decrease in the monoclinic β angle and an increase in unit cell volume (Figures S11–12). At ~1423 °C, an additional reflection was observed between the $(11\bar{1})$ and (111) reflections of the *P*2/*c* phase. This reflection was fitted through the introduction of the tetragonal $I4_1/a$ scheelite-type phase. Additional reflections between 40–60 ° 2θ were observed upon further heating, and these were also fitted to the $I4_1/a$ phase.

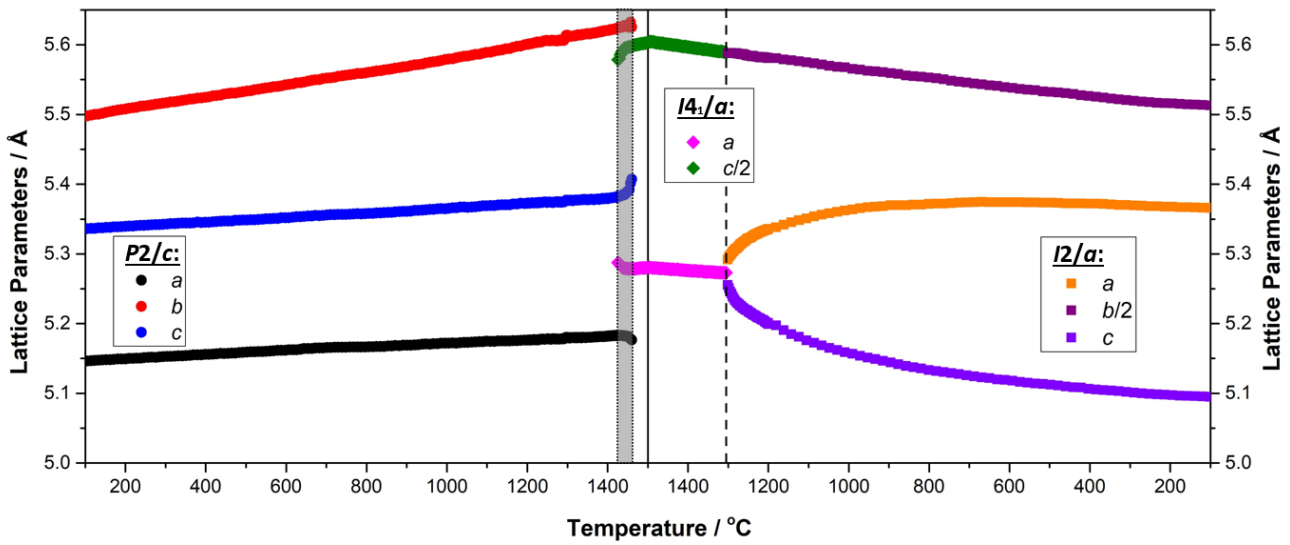

Figure 6: Temperature dependence of the unit cell parameters for $HoTaO_4$ obtained by Rietveld refinements against neutron powder diffraction data. The data were collected as the sample was heated from room temperature to 1500 °C, then cooled to room temperature. For ease of comparison, the unit cell parameters of the *I*-centered cell have been appropriately rescaled. The error bars are smaller than the symbols. The two-phase region is indicated by a grey shaded area, whereas the phase transition upon cooling is indicated by a dashed line.

The reflections from the $I4_1/a$ phase continued to grow in intensity as those from the $P2/c$ phase decreased, indicating that a first order phase transition was occurring. The corresponding two-phase model was refined until the peaks around 21–26 ° and the intense peak between 50–53 ° 2θ were indistinguishable from the background. This was observed to be ~1464 °C, after which a single phase tetragonal $I4_1/a$ model was refined until 1500 °C. The phase fraction of the $P2/c$ and $I4_1/a$ phases is plotted in Figure 7. Isothermal measurements were conducted at the highest investigated temperature for one hour, and the diffraction data showed no significant changes over this time, indicating the samples rapidly reached equilibrium.

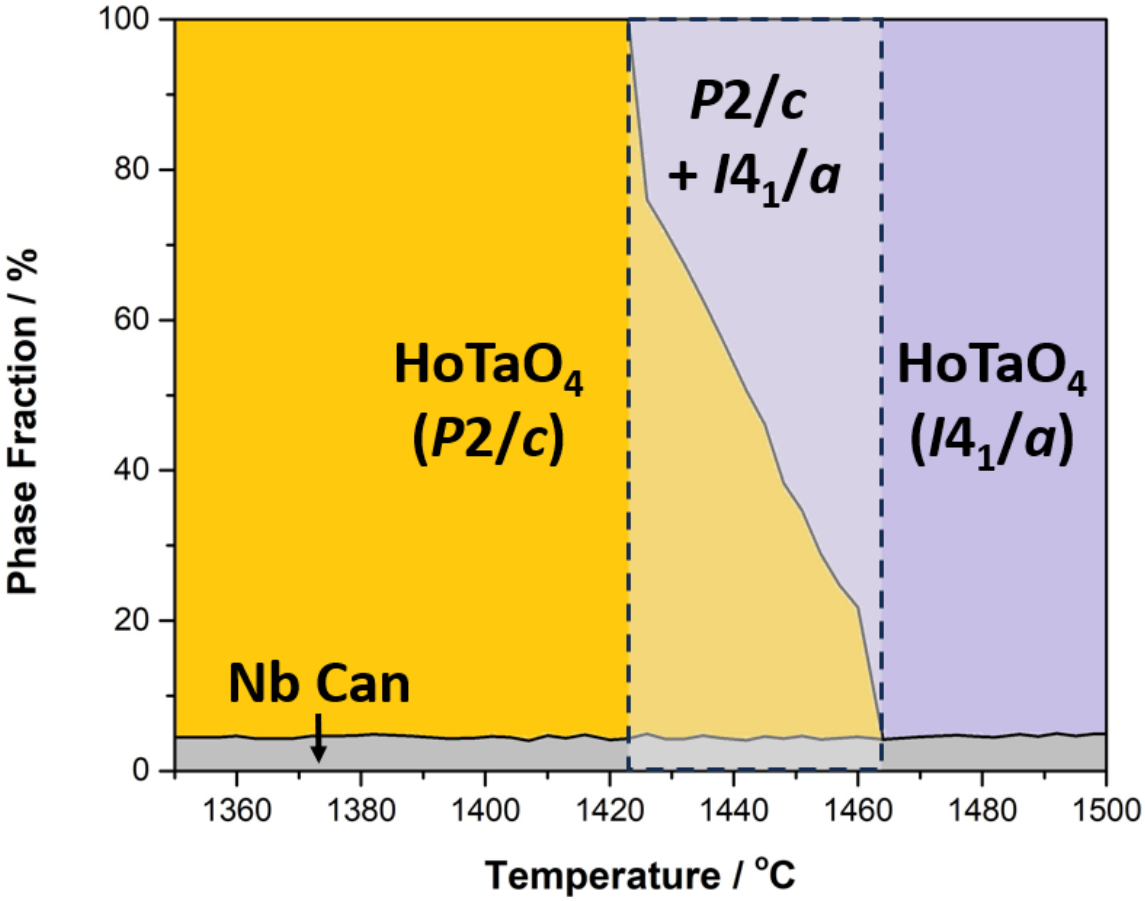

Figure 7: Phase fraction of the two-phase first order phase transition in $HoTaO_4$ upon heating. The two-phase region is highlighted in the shaded area.

Upon cooling, the tetragonal $I4_1/a$ phase displayed unsurprising lattice contraction. At ~1300 °C, additional reflections began to emerge around 45–60 ° 2θ. These reflections appeared in different ranges to those observed for the $P2/c$ phase, indicating that $HoTaO_4$ was transitioning to a different phase upon cooling. The additional reflections were fitted following the introduction of a monoclinic $I2/a$ phase to the refinement model. This phase transition occurred without a two-phase region, indicating it is possibly continuous in nature. However, a similar Landau mean-field theory analysis of the strain components and monoclinic β angle demonstrated that the phase transition was not strictly second order or tricritical, with the critical exponent $\beta = 0.370$ and $T_c = 1301$ °C for ϵ_6 (Figures S13–15). The $P2/c$ phase was not detected upon cooling, indicating that the monoclinic $P2/c$ to tetragonal $I4_1/a$ phase transition is irreversible. The $I4_1/a$ to $I2/a$ phase transition that occurred upon cooling very closely followed the behavior observed by $HoNbO_4$, despite occurring at almost twice the temperature, with similar anisotropic contraction of the unit cell parameters and an increase in the monoclinic β angle (Figure 6, and Figures S11–15).

(iii) *In Situ Neutron Diffraction Measurements of Ho_2O_3 + Ta_2O_5 Green Powder: Observation of an Intermediate $C222_1$ Phase*

NPD patterns were measured for the two starting reagents before a stoichiometric mixture of Ho_2O_3 and Ta_2O_5 was pressed as a rod, after ball milling to ensure adequate mixing of the two oxide powders. Rietveld analysis of the NPD patterns confirmed that both starting reagents were crystalline and single phase (Figure S16), with the expected stoichiometry also confirmed using X-ray fluorescence spectroscopy (Table S3).

At room temperature, Ho_2O_3 has a cubic structure (SG $Ia\bar{3}$, #206) with lattice parameter a = 10.623(4) Å, as reported previously.[68, 69] The structure of Ta_2O_5 is more complex. Previous X-ray studies of Ta_2O_5 have reported a reversible phase transition around 1360 °C, and earlier studies suggested that this structure is sensitive to the heat treatment of the material.[70] It was subsequently established that at room temperature Ta_2O_5 has an incommensurate modulated structure featuring distortion planes. Stephenson and Roth proposed that this could be adequately described by an 'average' orthorhombic unit cell in space group *P*2*mm* (#25) with *a*-, *b*-, and *c*-axis dimensions of 6.198 × 40.29 × 3.888 Å that contains 11 formula units with 12 unique Ta^{5+} and 33 unique O^{2-} positions.[70] As the present experiment used a medium resolution, high intensity neutron diffractometer, it was elected to use the average structure developed by Stephenson and Roth in the Rietveld refinements of the NPD data. In these refinements, the ADPs of the 12 unique Ta^{5+} cations were constrained to be equal, as were those of the 33 unique O^{2-} atoms. This resulted in an acceptable fit to the pattern measured at room temperature, and this model was employed in the subsequent variable temperature studies.

Analysis of the NPD patterns of the green powder measured as the temperature was increased from room temperature to 1500 °C revealed a series of transformations. To avoid overparameterization, several constraints were placed on the refinement process. A single B_{eq} was used for the cations of each phase, with a second value used for the oxygens in the same phase. No constraints were placed on the relative size of the ADPs between the separate phases. Due to the modest peak-shape resolution of the diffractometer, size and strain parameters were not refined.

The thermal evolution of the NPD can be separated into five stages upon heating, with an additional process evident upon cooling. These stages are depicted in Figure 8 and are summarized as follows:

Stage 1: Thermal expansion of Ho_2O_3 and Ta_2O_5 from room temperature to 1145 °C

Upon heating to 1145 °C, little change was initially seen in the diffraction patterns, and the only crystalline phases identified were the cubic Ho_2O_3 and orthorhombic Ta_2O_5 phases, together with reflections from the Nb can used to contain the sample. Both oxides showed conventional positive thermal expansion. A small decrease in the phase fraction of Nb was detected upon heating, presumably due to sintering and/or increasing crystallinity of the metal oxide. Normalized lattice parameters are shown in Figure S17. The Rietveld refinements demonstrate that both Ho_2O_3 and Ta_2O_5 remain unreacted below 1145 °C.

Stage 2: Emergence of a $HoTaO_4$ *P*2/*c* phase from ~1145 °C

Heating above 1145 °C resulted in changes to the relative intensities of several reflections, as well as additional reflections that could not be fitted using the three phase (Ho_2O_3, Ta_2O_5, and Nb) model employed in Stage 1. This was most apparent in the ~20–50 ° 2θ region where the relatively strong reflection at ~22 ° 2θ from the Ta_2O_5 phase began to lose intensity, and additional reflections emerged at ~29 and ~52 ° 2θ. These additional reflections were sharp, indicating the formation of a new crystalline phase. These reflections were fitted using a *P*2/*c* monoclinic phase, corresponding to $HoTaO_4$, and inclusion of this in the Rietveld refinements lowered the R_{wp} value (from 4.92% to 4.39% at 1145 °C), indicating a better fit to the data. The phase fractions of Ho_2O_3 and Ta_2O_5 were observed to decrease, while the phase fraction of $HoTaO_4$ (*P*2/*c*) increased. This indicated that the reaction between the two metal oxides began around 1145 °C.

Stage 3: Emergence of the weberite-type Ho_3TaO_7 at 1200 °C

Further heating to ~1200 °C resulted in more reflections emerging that could not be fit to the four-phase model (Ho_2O_3 + Ta_2O_5 + *P*2/*c* $HoTaO_4$ + Nb). The appearance of these new reflections was accompanied by a noticeable reduction in the intensity of the most prominent reflections from Ho_2O_3, indicating a reaction to form an additional phase was occurring. Examination of the Inorganic Crystal Structure Database (ICSD) for other materials in the Ho_2O_3–Ta_2O_5 phase diagram suggested the possibility of a weberite-type Ho_3TaO_7 structure. Three different space groups have been reported for weberite-type tantalates, depending on the size of the *A*-site cation and synthesis conditions. The larger lanthanoids (A^{3+} = La–Nd) are reported to adopt an orthorhombic structure in the *Cmcm* space group, whereas the $C222_1$ space group is favored for

the remainder of the lanthanoids (noting that a cubic structure in $Fm\bar{3}m$ has been described for A^{3+} = Ho).[71] Both structures were tested and were found to give similar quality of fits. Since previous work by Gussev *et al.* has shown the need for neutron total scattering measurements to differentiate between these closely related structures, the $C222_1$ space group structure was adopted in line with their suggestion.[72, 73] The addition of this phase to the refinement model successfully accounted for the additional reflections, and at ~1234 °C the sample is a mixture of $HoTaO_4$ ($P2/c$) and Ho_3TaO_7 together with unreacted Ta_2O_5. Further heating resulted in a gradual decrease in the intensity of the reflections from Ta_2O_5 and these became indistinguishable from the background at around ~1340 °C.

The formation of Ho_3TaO_7 is unusual. The orthorhombic weberite-type structure is an ordered A_3BO_7 superstructure of fluorite, formed by a combination of cation ordering and the presence of anion vacancies.[72] Previous studies have suggested that final annealing temperatures between 1200-1350 °C are necessary to successfully synthesize this phase.[71, 72] These annealing temperatures are in line with the current *in situ* measurements, as the formation of Ho_3TaO_7 from Ho_2O_3 and Ta_2O_5 reagents occurs within this temperature range (Figure 8). The weberite-type phase also forms with little temperature dwell time, in line with other solid state synthesis *in situ* studies of similar materials.[74]

Stage 4: Two-phase region of $HoTaO_4$ ($P2/c$) and weberite-type Ho_3TaO_7 from 1340–1390 °C

With continued heating, the phase fraction of Ho_3TaO_7 decreases while that of $HoTaO_4$ ($P2/c$) increases until ~1390 °C, where peaks diagnostic of Ho_3TaO_7 become indistinguishable from the background. The fact that neither the reagent metal oxide, nor Ho_3TaO_7, are detected *in situ* above 1390 °C matches with previous *ex situ* studies that found pure $HoTaO_4$ ($P2/c$ structure) formed upon cooling after annealing at 1400 °C for 48 hours.[55]

Stage 5: Conversion to the high temperature $HoTaO_4$ ($I4_1/a$) phase from 1390 °C

Heating the sample above 1390 °C results in the appearance of weak reflections diagnostic of the tetragonal scheelite-type structure. There is a wide temperature window from 1390-1450 °C in which the two phases ($P2/c$ and $I4_1/a$) coexist, similar to that described above in Part ii. The large two-phase region indicates this transformation is sluggish, suggesting that incomplete conversion of $P2/c$ to $I4_1/a$ is possible. This was previously seen in an *ex situ* heating study of $ErTaO_4$, where a mixed $I2/a$ + $P2/c$ sample was recovered upon cooling to room temperature.[49] Further heating of the sample results in the complete conversion to the $I4_1/a$ scheelite-type structure around ~1450

°C, and Rietveld refinement showed this to be phase pure to 1500 °C (with the exception of the Nb can). This is in line with previous *ex situ* observations.[55]

Stage 6: Cooling the high temperature $HoTaO_4$ ($I4_1/a$) phase back to $HoTaO_4$ ($I2/a$)

After heating the green powder to 1500 °C, the sample was maintained at this temperature for four hours before being cooled to near room temperature. NPD data were collected during the cooling and the patterns displayed very similar characteristics to that described in Part ii of this manuscript for $HoTaO_4$. The sample transformed from the high temperature $I4_1/a$ structure to the low temperature $I2/a$ phase at ~1300 °C, Figure S18.7

It is interesting to note that, as described in Part ii above, the $I2/a$ phase was only observed upon cooling from the $I4_1/a$ structure and was not evident at any stage during the heating of the Ho_2O_3 + Ta_2O_5 green powder. The inability of the $I4_1/a$ structure to cool back into the $P2/c$ structure was described by Graham, where a rotational twinning between the two structures was identified.[75] Graham further stated there is no simple mechanism to facilitate this transformation, meaning the higher energy metastable $I2/a$ state is preferentially formed upon cooling. This has also been found in computational studies, where for $HoTaO_4$ the $P2/c$ phase was found to have a lower ground state energy than the $I2/a$ structure.[55] Our data supports these findings.

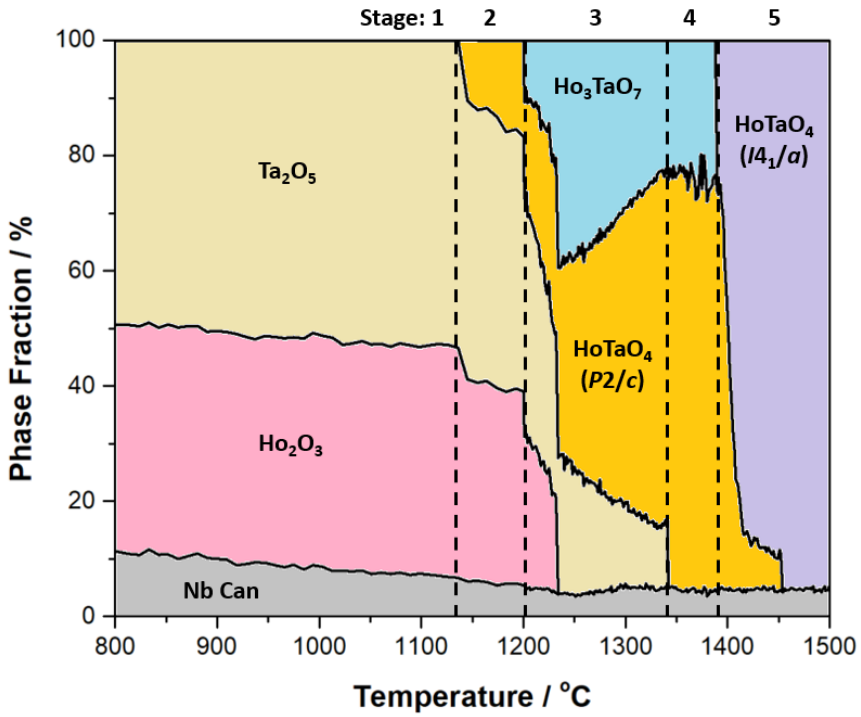

Figure 8: Refined phase fraction values extracted from *in situ* neutron powder diffraction studies of the Ho_2O_3 and Ta_2O_5 green powder as a function of temperature. For clarity, data below 800 °C is not shown. Samples were rapidly heated (180 °C hr^{-1}) to 1200 °C before being slowly heated (30 °C hr^{-1}) to 1500 °C.

(iv) *Ionic Conductivity Studies of P2/c and I2/a Fergusonite-Type Structures*

The conductivities of $HoNbO_4$ and $HoTaO_4$ were measured using EIS in the temperature range of 850–600 °C under different atmospheres (air, Ar, wet Ar, and wet 5% H_2 in Ar). Each ionic conductivity measurement was performed over a period of 5 minutes after thermally equilibrating the sample for 20 minutes to ensure sufficient diffusion time for defect stabilization. This is significantly longer than the NPD experiment where datasets were collected every four minutes. Although defects are expected to be small in number and have limited impact on the structure established using neutron diffraction, they are crucial in conductivity measurements. Measurements in wet conditions were performed with extremely slow cooling ramps (*i.e.*, -10 ° hr^{-1}, rather than -200 ° hr^{-1} for dry tests) to provide extra time for proton incorporation into the bulk of the dense pellets. Further verification of defect stabilization was performed by repeating EIS acquisitions after an additional 20 minutes at 800 °C, 700 °C, and 600 °C by introducing a 0.1 V bias. No significant differences between the results with or without bias were observed, also confirming the results fall within the linear domain of the *I*/*V* curves. After collecting the data in wet hydrogen, the measurements in air were systematically repeated to verify the sample stability and to regenerate the Pt cables and electrodes. Comparing the two measurements showed good data reproducibility and, therefore, excellent reliability. The resulting impedance spectra were fitted by the equivalent circuit method (ECM) to analyze the resistive contributions.

A single contribution composed of a resistance (R) in parallel with a constant phase element (CPE) is necessary to fit the $HoNbO_4$ and $HoTaO_4$ (*I*2/*a*) results. Conversely, the $HoTaO_4$ (*P*2/*c*) fitting requires two R//CPE contributions. Nyquist plots at 850 °C reporting the EIS data normalized over geometrical parameters of the pellets, along with the ECM models and fitting results for all the samples in different gas conditions, are presented in Figure S19. Warburg spikes are not observed as the large magnitude of the resistivity dominates the contribution of ion diffusion towards the electrode interface. To associate the resistive contributions with physical phenomena, the equivalent capacitances were calculated for each contribution.[76] The high-frequency contributions present capacitances between 10^{-11} and 10^{-12} F cm^{-1}, identifying them as bulk resistances.[77] A single high-frequency contribution is present for $HoNbO_4$ and $HoTaO_4$ (*I*2/*a*), meaning that bulk resistances dominate the conduction. For $HoTaO_4$ (*P*2/*c*), a second resistive contribution is observed in a similar frequency range. This second contribution presents comparable capacitances to the first (0.5–1.0 × 10^{-11} F cm^{-1}) in air, Ar, and wet Ar. Since the activation energies are similar, the two phenomena are considered bulk resistivities. Conversely, results in wet 5% H_2 in Ar show larger capacitance values for the second contribution (5–8 × 10^{-8} F cm^{-1}), suggesting the contribution of grain boundary resistivity.[77] However, the subtraction

of this grain boundary contribution does not influence the total resistivity as the bulk contribution dominates the conduction.

The total conductivity of each sample was calculated using the resistance extracted from the equivalence circuit method in the respective Nyquist plots (Figure S19). The results are reported in Figure 9 as Arrhenius plots with the conductivity presented on a logarithmic scale. The conductivity values obtained were 10^{-5}–10^{-8} S cm^{-1} within the 850–585 °C temperature range for all gas environments. The results show an exponential reduction with a decrease in temperature typical of thermally activated processes such as ionic diffusivity. The activation energies were calculated from linear fits to the Arrhenius plots.

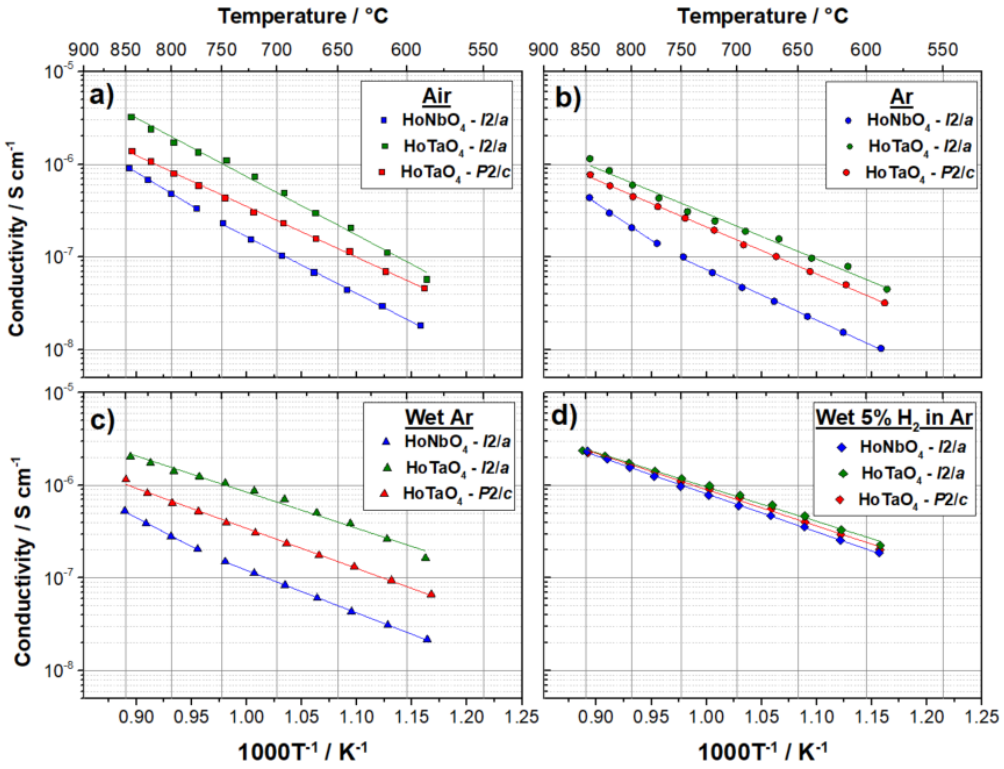

Figure 9: Conductivity results of $HoNbO_4$ *I*2/*a* (filled blue symbols), $HoTaO_4$ *I*2/*a* (filled green symbols), and $HoTaO_4$ *P*2/*c* (filled red symbols) in Arrhenius plots with a logarithmic scale as a function of the inverse of the temperature measured at 600-850 °C in (a) air, (b) Ar, (c) wet Ar, and (d) wet 5% H_2 in Ar.

The conductivity values are in line with other undoped *Ln*NbO_4 compounds.[22, 31, 78, 79] $LaNbO_4$ presents conductivity of ~10^{-5} S cm^{-1} at 800 °C in wet H_2.[80] The conductivity of undoped *A*WO_4 (A^{2+} = Sr, Ba) is ~10^{-7} S cm^{-1} at 800 °C in wet H_2, while *A*MoO_4 (A^{2+} = Ca, Sr, Ba) reaches as high as 10^{-4} S cm^{-1}.[4, 16] The Mo- and W-based *AB*O_4 compounds also present activation energies higher than 1 eV. Although these values are insufficient for practical application in SOFCs, the possibility of doping and

short synthesis times makes these compounds a promising framework for structural modifications. Under dry conditions, the highest conductivities were observed for $HoTaO_4$ (*I*2/*a*), followed by $HoTaO_4$ (*P*2/*c*) and $HoNbO_4$ (*I*2/*a*), reaching 3.2, 1.4, and 0.9 × 10^{-6} S cm^{-1} in air at 850 °C respectively. Slightly larger values are observed in air compared to Ar at high temperatures (Figure 10). This may suggest a possible *p*-type conductivity contribution that becomes negligible below 600 °C. Results in wet Ar (Figure 9c) show an increase compared to dry Ar, attributed to the proton conductivity contribution. The same trend in conductivity is observed in both wet and dry Ar [*i.e.*, $HoTaO_4$ (*I*2/*a*) > $HoTaO_4$ (*P*2/*c*) > $HoNbO_4$ (*I*2/*a*)]. The maximum value of 8.9 × 10^{-7} S cm^{-1} is obtained for $HoTaO_4$ (*I*2/*a*) at 850 °C. Evidently, changing the *B*-site cation from Nb^{5+} to Ta^{5+} increases the conductivity of the *I*2/*a* phase. Furthermore, the conductivities in wet H_2 in Ar are essentially identical for the three samples (Figure 9d) and reach a maximum of 2.4 × 10^{-6} S cm^{-1} at 850 °C. Comparing the conductivities as a function of the gas environment highlights the variation between reducing and oxidizing conditions for each sample (Figure 10). The notable increase of conductivity under reducing conditions suggests the presence of *n*-type conductivity contribution. A possible explanation for the observed *n*-type conductivity in these phases is the partial reduction of the Nb^{5+}/Ta^{5+} cations, which is favored by the underbonding of the *B*-site cation. Further studies are necessary to confirm this hypothesis. Such electronic conduction should be avoided to fully exploit the electrical potential for the ionic/protonic transfer.

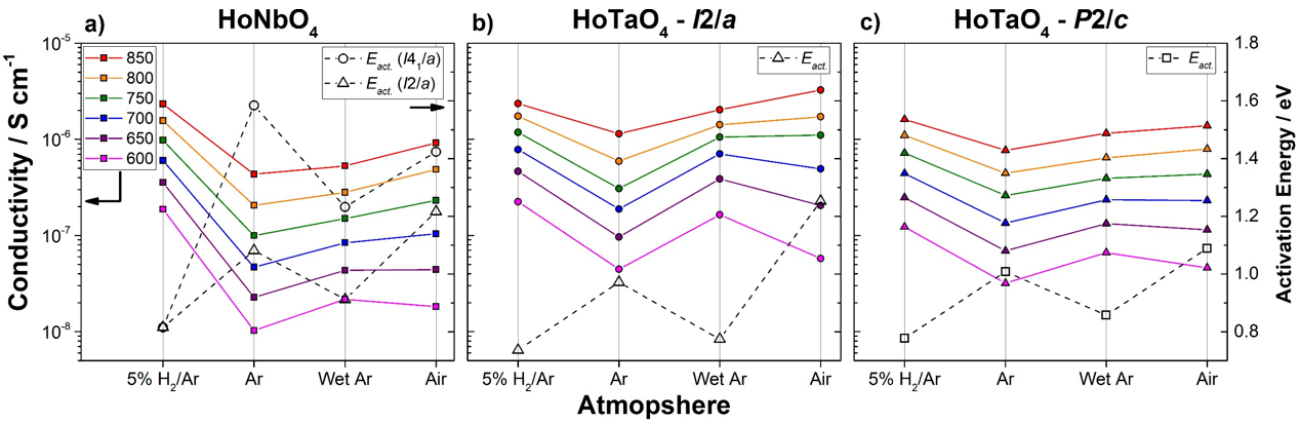

Figure 10: Conductivity results on a logarithmic scale (left axis) and activation energy (right scale) as a function of the atmosphere measured from 850-600 °C for (a) $HoNbO_4$, (b) $HoTaO_4$ *I*2/*a*, and (c) $HoTaO_4$ *P*2/*c*. For $HoNbO_4$ that exhibits a phase transition, the activation energy of both the *I*2/*a* and $I4_1/a$ phases are plotted.

Both phases of $HoTaO_4$ (*I*2/*a* and *P*2/*c*) show linear Arrhenius plots under all the investigated atmospheres. A change in the slope of the Arrhenius plot was observed for $HoNbO_4$ in the measurements conducted in air, Ar, and wet Ar around 775 °C associated with the *I*2/*a* to $I4_1/a$ phase transition. The high temperature phase ($I4_1/a$) has a higher activation energy, in contrast to the initial hypothesis that the conductivity will be greater in the high temperature tetragonal phase because of the Nb^{5+} underbonding. The increase of the activation energy ($E_{act.}$) above the phase transition is contrary to the literature results for pure and *A*-site doped $LaNbO_4$, suggesting the size of the *A*-site cation may play a role as Ho^{3+} is smaller than La^{3+}.[22, 31, 81] A corresponding change in slope was not observed for $HoTaO_4$ materials as the phase transition occurs at a much higher temperature than the measured ionic conductivity range (Figure 6). Although measuring the conductivity across the *P*2/*c*–$I4_1/a$ phase transition of $HoTaO_4$ would be interesting, the experimental procedure is extremely challenging.[82, 83] In addition, the phase transition temperature of 1300 °C is outside the moderate SOFC operating temperature of 500–750 °C.

The atmosphere dependent $E_{act.}$ values are illustrated in Figure 10 (and listed in Table S4). Figure 10a contains an additional curve for $HoNbO_4$ showing both the monoclinic *I*2/*a* and tetragonal $I4_1/a$ phases. A remarkable increase in $E_{act.}$ was observed for the tetragonal phase under all gaseous environments except for wet 5% H_2 in Ar, for which the $E_{act.}$ Of both phases are equal. The lowest value of $E_{act.}$ for $HoNbO_4$ is found in wet hydrogen (0.82 eV). This is similar to the trend observed for the two $HoTaO_4$ phases (0.74 and 0.78 eV for *I*2/*a* and *P*2/*c* respectively). For all samples, a slight increase in $E_{act.}$ is observed in wet Ar with respect to H_2, with the values increasing further under Ar, and finally reaching a maximum $E_{act.}$ in air. That adding water to the gases systematically reduces $E_{act.}$ Is a clear indication of protonic conductivity. Although the $E_{act.}$ values are quite large,[84] the $E_{act.}$ of proton conductivity contribution in Ar, calculated as the difference between wet and dry Ar conductivities, are between 0.64–0.71 eV. These values are similar to the E_{act} of pure bulk proton conductivity around 0.5 eV.[85] This suggests that the activation energy of the tetragonal $I4_1/a$ phase of $HoNbO_4$ is larger than that of the monoclinic *I*2/*a* phase, possibly suggesting stabilization of the low temperature phase is preferable for ionic conductivity applications.

The existence of proton conductivity and a lack of phase transition in the undoped phases is a promising indication to consider *Ln*TaO_4 materials as a framework for further modifications. A possible strategy to improve conductivity by acceptor doping was proposed by Haugsrud *et al*. and Norby *et al.* for $LaNbO_4$.[15, 24, 25, 86] The introduction of acceptor dopants increases the number of positive point defects (mainly oxygen vacancies) due to charge compensation, resulting in an enhancement of conductivity. These oxygen vacancies are filled during water incorporation by

hydroxide ions ($OH_O^{\cdot}$) with protons in the interstitial positions. Proton diffusion occurs *via* the Grotthuss mechanism through inter-and intra-tetrahedral hopping of $H_i^{\cdot}$ bonded to oxygens. For $LaNbO_4$, proton migration is limited by the inter-tetrahedral step, and the addition of dopants may also introduce potential sites for proton trapping.[24] Therefore, the fact that the intrinsic defects in $HoTaO_4$ are mostly interstitial oxygens may contribute additional migration paths for proton hopping that are alternatives to the inter-tetrahedra ones. Increasing interstitial oxygen *via* doping small hexavalent cations is a viable option to enhance proton conductivity whilst limiting the proton trapping effect.

Finally, an analysis of the potential conduction pathways was undertaken based on the structures obtained from NPD. Previous studies have highlighted the potential for oxygen ions to move *via* interstitial sites within ABO_4-type materials.[35, 87, 88] Huse *et al.* identified a correlation between ionic conductivity and the O–O distances separating the different NbO_6 polyhedra in $LaNbO_4$.[60] A similar analysis was conducted with the O(1)–O(1) and O(1)–O(2) distances determined from the study of the NPD data, used to estimate the size of the conduction pathway (Figure S20). These values are presented (Table S8) and show a correlation between the average O–O distance and activation energy in air (Figure S21). Evidently, the conclusions drawn by Huse *et al.* extend to other $LnNbO_4$ and $LnTaO_4$ oxides. Mullens *et al.* previously highlighted that in $LnBO_4$ (B^{5+} = Nb, Ta) structures, the Nb^{5+} and Ta^{5+} cations are at slightly different positions in the isostructural $I2/a$ phases due to the differences in the 4*d* and 5*d* orbitals.[49] This leads to a larger *B*–*B* separation in B^{5+} = Ta compared to Nb, potentially contributing to the higher ionic conductivity exhibited in the $HoTaO_4$ structures. The conductivity pathway is different in the $P2/c$ structure as a consequence of the different arrangement of the TaO_6 chains (Figure 1), potentially explaining the difference in conductivity between the $I2/a$ and $P2/c$ structures. Further studies of other $LnTaO_4$ materials in both the $I2/a$ and $P2/c$ space groups are required to confirm this.

Conclusions

The present study of the variable temperature structure evolution of the two oxides $HoNbO_4$ and $HoTaO_4$ establishes a number of important facts. Firstly, the monoclinic *I*2/*a* to tetragonal *I*4$_1$/*a* phase transition is not strictly second order in either oxide, with the larger displacement of the cations from their high symmetry equivalent position correlated with both the magnitude of the monoclinic distortion and the transition temperature. Secondly, a second monoclinic polymorph of $HoTaO_4$, described in the *P*2/*c* space group, can be isolated, and the transition of this structure to the tetragonal *I*4$_1$/*a* structure at ~1300 °C is clearly first order with the two phases coexisting over an extended temperature range. This transition is irreversible, and cooling the sample results in the formation of the higher energy *I*2/*a* polymorph. Neither $HoTaO_4$ nor $HoNbO_4$ exhibits classical Landau mean field-type behavior far from the *I*2/*a* to *I*4$_1$/*a* phase transition, suggesting these transformations are not entirely second order and their presence below the operating temperature of SOFCs will potentially restrict their use as ionic conductors.

Heating a mixture of Ho_2O_3 + Ta_2O_5 results in a complex series of reactions and provides the first direct evidence for the formation of a weberite-type Ho_3TaO_7 intermediate. *In situ* methods showed that the *I*2/*a* phase only forms upon cooling from the high temperature tetragonal *I*4$_1$/*a* phase. That the Ho_3TaO_7 phase only exists between 1200–1390 °C suggests a possible strategy for the formation of this phase, using solid state methods with minimal heating dwell time. Interestingly, the analogous Ho_3NbO_7 compound does not appear to have been reported in the literature, and it is of interest to establish if this can be observed using fast *in situ* measurements to aid understanding of the differences between Nb^{5+} and Ta^{5+}.[89]

Surprisingly, the activation energy for $HoNbO_4$ was found to be higher in the high temperature tetragonal *I*4$_1$/*a* phase than in the low temperature monoclinic *I*2/*a* phase, suggesting future studies of ionic conductors should focus on the stabilization of the low-temperature monoclinic phase. Replacing Nb^{5+} with Ta^{5+} exhibits great promise for potential ionic conductor studies, as the potentially detrimental phase transition occurs well above the proposed operating temperature of SOFCs. This study further identified tunable characteristics key to improving the mobility of charge carriers within these *AB*O_4 structures, such as large *A*-site cations to 'open up' the O–O channels within the structure, avoiding phase transitions to the high-temperature tetragonal *I*4$_1$/*a* structure, and the use of Ta^{5+} on the *B* site to increase the *B*–*B* separation. Once the mobility of the charge carriers is optimized within this structural framework, future work can focus on increasing the number of charge carriers by either inducing oxygen vacancies (by substituting Ta^{5+} for Fe^{4+}, Ge^{4+}, or Si^{4+} for example) or inducing

additional interstitial oxygen ions (by substituting Ta^{5+} for Mo^{6+} or W^{6+} for example). As there are limited ionic conductivity studies concerned with Ta-containing metal oxides, this presents a possible direction in designing new robust ionic conductors for SOFCs that exhibit excellent conductivity and stability in harsh environments.

Conflicts of Interest

There are no conflicts of interest to declare.

Supporting Information

The supporting information if available, free of charge, at XXX.

The furnace program and ramp rates used for variable temperature neutron diffraction. Full refinement parameters for $HoNbO_4$ and $HoTaO_4$ polymorphs, Landau mean-field theory analysis of $HoTaO_4$ upon cooling, and further ionic conductivity data.

Acknowledgements

We acknowledge the support of the Australian Research Council for this work that was facilitated by access to Sydney Analytical, a core research facility at the University of Sydney and was, in part, undertaken at the Australian Centre for Neutron Scattering (P9760). Bryce G. Mullens thanks the Australian Institute for Nuclear Science and Engineering for a PGRA and SAAFE scholarship. M.S.-M. gratefully acknowledges the financial support from Comunidad de Madrid, Spain, through an "Atracción de Talento Investigador" fellowship (2020-T2/IND-20581).

References

1. Brett, D. J.; Atkinson, A.; Brandon, N. P.; Skinner, S. J., Intermediate temperature solid oxide fuel cells. *Chemical Society Reviews* **2008,** *37* (8), 1568-1578.
2. Shi, H.; Su, C.; Ran, R.; Cao, J.; Shao, Z., Electrolyte materials for intermediate-temperature solid oxide fuel cells. *Progress in Natural Science: Materials International* **2020,** *30* (6), 764-774.
3. Shahid, M., Recent advances in protonconducting electrolytes for solid oxide fuel cells. *Ionics* **2022,** *28* (8), 3583-3601.
4. Afif, A.; Zaini, J.; Rahman, S. M. H.; Eriksson, S.; Islam, M. A.; Azad, A. K., Scheelite type $Sr_{1-x}Ba_xWO_4$ (x = 0.1, 0.2, 0.3) for possible application in solid oxide fuel cell electrolytes. *Scientific Reports* **2019,** *9* (1), 1-10.
5. Canu, G.; Giannici, F.; Chiara, A.; Confalonieri, G.; Longo, A.; Buscaglia, M. T.; Dapiaggi, M.; Buscaglia, V.; Martorana, A., Characterisation of scheelite $LaW_{0.16}Nb_{0.84}O_{4.08}$ ion conductor by combined synchrotron techniques: Structure, W oxidation state and interdiffusion. *Journal of Alloys and Compounds* **2021,** *857*, 157532.
6. Kowalkińska, M.; Głuchowski, P.; Swebocki, T.; Ossowski, T.; Ostrowski, A.; Bednarski, W.; Karczewski, J.; Zielińska-Jurek, A., Scheelite-type wide-bandgap ABO_4 compounds (A = Ca, Sr, and Ba; B = Mo and W) as potential photocatalysts for water treatment. *The Journal of Physical Chemistry C* **2021,** *125* (46), 25497-25513.
7. Sahmi, A.; Omeiri, S.; Bensadok, K.; Trari, M., Electrochemical properties of the scheelite $BaWO_4$ prepared by co-precipitation: Application to electro-photocatalysis of ibuprofen degradation. *Materials Science in Semiconductor Processing* **2019,** *91*, 108-114.
8. Liu, Y.; Jia, D.; Zhou, Y.; Zhou, Y.; Zhao, J.; Li, Q.; Liu, B., Discovery of ABO_4 scheelites with the extra low thermal conductivity through high-throughput calculations. *Journal of Materiomics* **2020,** *6* (4), 702-711.
9. Bsaibess, E.; Delorme, F.; Monot-Laffez, I.; Giovannelli, F., Ultra-low thermal conductivity in scheelite and A-deficient scheelite ceramics. *Scripta Materialia* **2021,** *201*, 113950.
10. Tabuteau, A.; Pages, M., Identification and crystal chemistry of double molybdates of alkali metals (K, Rb, Cs) and transuranium elements (Np, Pu, Am). *Journal of Inorganic and Nuclear Chemistry* **1980,** *42* (3), 401-403.
11. Fonteneau, G.; L'Helgoualch, H.; Lucas, J., Les niobates $CaUNb_2O_8$ et $MThNb_2O_8$ (M = Ca, Sr, Cd). Etude des transformations monoclinique-quadratique. *Materials Research Bulletin* **1977,** *12* (1), 25-33.
12. Bastide, J., Simplified systematics of the compounds ABX_4 ($X = O^{2-}, F^-$) and possible evolution of their crystal-structures under pressure. *Journal of Solid State Chemistry* **1987,** *71* (1), 115-120.
13. Chay, C.; Avdeev, M.; Brand, H. E.; Injac, S.; Whittle, T. A.; Kennedy, B. J., Crystal structures and phase transition behaviour in the 5*d* transition metal oxides $AReO_4$ (A = Ag, Na, K, Rb, Cs and Tl). *Dalton Transactions* **2019,** *48* (47), 17524-17532.
14. Kennedy, B. J.; Injac, S.; Thorogood, G. J.; Brand, H. E.; Poineau, F., Structures and phase transitions in pertechnetates. *Inorganic Chemistry* **2019,** *58* (15), 10119-10128.
15. Haugsrud, R.; Norby, T., High-temperature proton conductivity in acceptor-doped $LaNbO_4$. *Solid State Ionics* **2006,** *177* (13-14), 1129-1135.
16. Arab, M.; Lopes-Moriyama, A. L.; dos Santos, T. R.; de Souza, C. P.; Gavarri, J. R.; Leroux, C., Strontium and cerium tungstate materials $SrWO_4$ and $Ce_2(WO_4)_3$: Methane oxidation and mixed conduction. *Catalysis Today* **2013,** *208*, 35-41.
17. Cao, Y.; Duan, N.; Wang, X.; Chi, B.; Jian, L., Enhanced electrical conductivity of Mo-doped $LaNbO_4$. *Journal of the European Ceramic Society* **2015,** *35* (6), 1979-1983.
18. Li, C.; Pramana, S. S.; Skinner, S. J., Room temperature structure and transport properties of the incommensurate modulated $LaNb_{0.88}W_{0.12}O_{4.06}$. *Dalton Transactions* **2019,** *48* (5), 1633-1646.

19. Toyoura, K.; Sakakibara, Y.; Yokoi, T.; Nakamura, A.; Matsunaga, K., Oxide-ion conduction *via* interstitials in scheelite-type $LaNbO_4$: A first-principles study. *Journal of Materials Chemistry A* **2018,** *6* (25), 12004-12011.
20. Mather, G. C.; Fisher, C. A.; Islam, M. S., Defects, dopants, and protons in $LaNbO_4$. *Chemistry of Materials* **2010,** *22* (21), 5912-5917.
21. Auckett, J. E.; Lopez-Odriozola, L.; Clark, S. J.; Evans, I. R., Exploring the nature of the fergusonite-scheelite phase transition and ionic conductivity enhancement by Mo^{6+} doping in $LaNbO_4$. *Journal of Materials Chemistry A* **2021,** *9* (7), 4091-4102.
22. Li, C.; Bayliss, R. D.; Skinner, S. J., Crystal structure and potential interstitial oxide ion conductivity of $LnNbO_4$ and $LnNb_{0.92}W_{0.08}O_{4.04}$ (*Ln* = La, Pr, Nd). *Solid State Ionics* **2014,** *262*, 530-535.
23. Li, C.; Pramana, S. S.; Bayliss, R. D.; Grey, C. P.; Blanc, F.; Skinner, S. J., Evolution of structure in the incommensurate modulated $LaNb_{1-x}W_xO_{4+x/2}$ (x = 0.04–0.16) oxide ion conductors. *Chemistry of Materials* **2020,** *32* (6), 2292-2303.
24. Norby, T.; Magrasó, A., On the development of proton ceramic fuel cells based on Ca-doped $LaNbO_4$ as electrolyte. *Journal of Power Sources* **2015,** *282*, 28-33.
25. Haugsrud, R.; Norby, T., Proton conduction in rare-earth ortho-niobates and ortho-tantalates. *Nature Materials* **2006,** *5* (3), 193-196.
26. Esaka, T., Ionic conduction in substituted scheelite-type oxides. *Solid State Ionics* **2000,** *136*, 1-9.
27. Esaka, T.; Mina-ai, T.; Iwahara, H., Oxide ion conduction in the solid solution based on the scheelite-type oxide $PbWO_4$. *Solid State Ionics* **1992,** *57* (3-4), 319-325.
28. Takai, S.; Shitaune, S.; Sano, T.; Kawaji, H.; Yabutsuka, T.; Esaka, T.; Yao, T., Defect structure and oxide ion conduction of potassium ion substituted $CaWO_4$. *Materials* **2018,** *11* (7), 1092.
29. Fabbri, E.; Pergolesi, D.; Traversa, E., Materials challenges toward proton-conducting oxide fuel cells: A critical review. *Chemical Society Reviews* **2010,** *39* (11), 4355-4369.
30. Packer, R.; Tsipis, E.; Munnings, C.; Kharton, V.; Skinner, S.; Frade, J., Diffusion and conductivity properties of cerium niobate. *Solid State Ionics* **2006,** *177* (19-25), 2059-2064.
31. Bi, Z.; Peña-Martínez, J.; Kim, J.-H.; Bridges, C. A.; Huq, A.; Hodges, J. P.; Paranthaman, M. P., Effect of Ca doping on the electrical conductivity of the high temperature proton conductor $LaNbO_4$. *International Journal of Hydrogen Energy* **2012,** *37* (17), 12751-12759.
32. Packer, R.; Skinner, S., Remarkable oxide ion conductivity observed at low temperatures in a complex superstructured oxide. *Advanced Materials* **2010,** *22* (14), 1613-1616.
33. Bayliss, R. D.; Pramana, S. S.; An, T.; Wei, F.; Kloc, C. L.; White, A. J. P.; Skinner, S. J.; White, T. J.; Baikie, T., Fergusonite-type $CeNbO_{4+\delta}$: Single crystal growth, symmetry revision and conductivity. *Journal of Solid State Chemistry* **2013,** *204*, 291-297.
34. Wang, J.; Zhou, L.; Wang, Y.; Xu, J.; Yang, X.; Kuang, X., Molecular dynamic simulation of interstitial oxide ion migration in $Pb_{1-x}La_xWO_{4+x/2}$ scheelite. *Journal of Solid State Chemistry* **2018,** *268*, 16-21.
35. Ferrara, C. M., A.; Ritter, C.; Malavasi, L.; Tealdi, C.; , Interstitial oxide ion migration in scheelite-type electrolytes: A combined neutron diffraction and computational study. *Journal of Materials Chemistry A* **2015,** *3*, 22258-22265.
36. Rooksby, H.; White, E., The structures of 1:1 compounds of rare earth oxides with niobia and tantala. *Acta Crystallographica* **1963,** *16* (9), 888-890.
37. Stubičan, V. S., High-temperature transitions in rare-earth niobates and tantaIates. *Journal of the American Ceramic Society* **1964,** *47* (2), 55-58.
38. David, W. I. F., The high-temperature paraelastic structure of $LaNbO_4$. *Materials Research Bulletin* **1983,** *18* (6), 749-756.
39. Kuroiwa, Y.; Muramoto, H.; Shobu, T.; Tokumichi, H.; Yamada, Y., Pretransitional phenomena at the first-order phase transition in $LaNbO_4$. *J. Phys. Soc. Jpn.* **1995,** *64* (10), 3798-3803.

40. Fjeld, H.; Toyoura, K.; Haugsrud, R.; Norby, T., Proton mobility through a second order phase transition: Theoretical and experimental study of $LaNbO_4$. *Physical Chemistry Chemical Physics* **2010,** *12* (35), 10313-10319.
41. Hara, K.; Sakai, A.; Tsunekawa, S.; Sawada, A.; Ishibashi, Y.; Yagi, T., A soft acoustic mode in the ferroelastic phase transition of $LaNbO_4$. *J. Phys. Soc. Jpn.* **1985,** *54* (3), 1168-1172.
42. Parlinski, K.; Hashi, Y.; Tsunekawa, S.; Kawazoe, Y., Computer simulation of ferroelastic phase transition in $LaNbO_4$. *J. Mater. Res.* **1997,** *12* (9), 2428-2437.
43. Arulnesan, S. W.; Kayser, P.; Kimpton, J. A.; Kennedy, B. J., Studies of the fergusonite to scheelite phase transition in *Ln*NbO_4 orthoniobates. *Journal of Solid State Chemistry* **2019,** *277*, 229-239.
44. Saura-Múzquiz, M. M., Bryce G.; Maynard-Casely, Helen E.; Kennedy, Brendan J.; , Neutron diffraction study of the monoclinic-tetragonal phase transition in $NdNbO_4$ and $NdTaO_4$. *Dalton Transactions* **2021,** *50*, 11485-11497.
45. Sarin, P.; Hughes, R. W.; Lowry, D. R.; Apostolov, Z. D.; Kriven, W. M., High-temperature properties and ferroelastic phase transitions in rare-earth niobates (*Ln*NbO_4). *Journal of the American Ceramic Society* **2014,** *97* (10), 3307-3319.
46. Tsunekawa, S.; Takei, H., Domain switching behaviour of ferroelastic $LaNbO_4$ and $NdNbO_4$. *J. Phys. Soc. Jpn.* **1976,** *40* (5), 1523-1524.
47. Shannon, R. D., Revised effective ionic radii and systematic studies of interatomic distances in halides and chalcogenides. *Acta Crystallographica Section A: Crystal Physics, Diffraction, Theoretical and General Crystallography* **1976,** *32* (5), 751-767.
48. Machida, M.; Murakami, S.; Kijima, T.; Matsushima, S.; Arai, M., Photocatalytic property and electronic structure of lanthanide tantalates, *Ln*TaO_4 (*Ln* = La, Ce, Pr, Nd, and Sm). *The Journal of Physical Chemistry B* **2001,** *105* (16), 3289-3294.
49. Mullens, B. G.; Saura-Múzquiz, M.; Marlton, F. P.; Avdeev, M.; Brand, H. E.; Mondal, S.; Vaitheeswaran, G.; Kennedy, B. J., Beyond the ionic radii: A multifaceted approach to understand differences between the structures of *Ln*NbO_4 and *Ln*TaO_4 fergusonites. *Journal of Alloys and Compounds* **2022,** *930*, 167399.
50. David, W. I. F., Transition temperature - Spontaneous strain - Atomic displacement relationships in ferroelastics. *Materials Research Bulletin* **1983,** *18* (7), 809-816.
51. Studer, A. J.; Hagen, M. E.; Noakes, T. J., Wombat: The high-intensity powder diffractometer at the OPAL reactor. *Physica B: Condensed Matter* **2006,** *385*, 1013-1015.
52. Coelho, A. A., TOPAS and TOPAS-Academic: An optimization program integrating computer algebra and crystallographic objects written in C++. *Journal of Applied Crystallography* **2018,** *51* (1), 210-218.
53. Thompson, P.; Cox, D.; Hastings, J., Rietveld refinement of Debye–Scherrer synchrotron X-ray data from Al_2O_3. *Journal of Applied Crystallography* **1987,** *20* (2), 79-83.
54. Momma, K.; Izumi, F., VESTA 3 for three-dimensional visualization of crystal, volumetric and morphology data. *Journal of Applied Crystallography* **2011,** *44* (6), 1272-1276.
55. Mullens, B. G.; Avdeev, M.; Brand, H. E. A.; Mondal, S.; Vaitheeswaran, G.; Kennedy, B. J., Insights into the structural variations in $SmNb_{1-x}Ta_xO_4$ and $HoNb_{1-x}Ta_xO_4$ combined experimental and computational studies. *Dalton Transactions* **2021,** *50*, 9103-9117.
56. Tsunekawa, S.; Kamiyama, T.; Sasaki, K.; Asano, H.; Fukuda, T., Precise structure analysis by neutron diffraction for *R*NbO_4 and distortion of NbO_4 tetrahedra. *Acta Crystallographica Section A: Foundations of Crystallography* **1993,** *49* (4), 595-600.
57. Brese, N.; O'Keeffe, M., Bond-valence parameters for solids. *Acta Crystallographica Section B: Structural Science* **1991,** *47* (2), 192-197.
58. Brown, I. D., Recent developments in the methods and applications of the bond valence model. *Chemical Reviews* **2009,** *109* (12), 6858-6919.

59. Kuang, X.; Green, M. A.; Niu, H.; Zajdel, P.; Dickinson, C.; Claridge, J. B.; Jantsky, L.; Rosseinsky, M. J., Interstitial oxide ion conductivity in the layered tetrahedral network melilite structure. *Nature Materials* **2008,** *7* (6), 498-504.
60. Huse, M.; Skilbred, A.; Karlsson, M.; Eriksson, S. G.; Norby, T.; Haugsrud, R.; Knee, C. S., Neutron diffraction study of the monoclinic to tetragonal structural transition in $LaNbO_4$ and its relation to proton mobility. *Journal of Solid State Chemistry* **2012,** *187*, 27-34.
61. Kondrat'eva, O.; Nikiforova, G.; Tyurin, A.; Khoroshilov, A.; Gurevich, V.; Gavrichev, K., Thermodynamic properties of, and fergusonite-to-scheelite phase transition in, gadolinium orthoniobate $GdNbO_4$ ceramics. *Journal of Alloys and Compounds* **2019,** *779*, 660-666.
62. Nikiforova, G.; Khoroshilov, A.; Gavrichev, K.; Knyazev, A.; Knyazeva, S., Fergusonite–Scheelite phase transition of praseodymium orthoniobate. *Inorganic Materials* **2019,** *55*, 964-967.
63. Salje, E. K.; Hayward, S. A.; Lee, W. T., Ferroelastic phase transitions: Structure and microstructure. *Acta Crystallographica Section A: Foundations of Crystallography* **2005,** *61* (1), 3-18.
64. Ishii, K.; Morita, N.; Nakayama, H.; Tsunekawa, S.; Fukuda, T., Raman spectra of $LaNbO_4$ in the ferroelastic phase and the relaxation after the state shift. *Physica Status Solidi (A)* **1989,** *112* (1), 207-214.
65. Gu, B.; Cummins, H.; Qiu, S.; Copic, M., Acoustic soft modes and the ferroelastic phase transition in $BiVO_4$ and $LaNbO_4$. *Ferroelectrics* **1983,** *52* (1), 45-57.
66. Wada, M.; Nakayama, Y.; Sawada, A.; Tsunekawa, S.; Ishibashi, Y., Raman scattering and fluorescence spectra of $LaNbO_4$. *J. Phys. Soc. Jpn.* **1979,** *47* (5), 1575-1580.
67. Tsunekawa, S.; Kamiyama, T.; Asano, H.; Fukuda, T., Relationship between covalence and displacive phase transition temperature in RAO_4 and $LiAO_3$ (R = rare-earth element and A = Nb and Ta). *Journal of Solid State Chemistry* **1995,** *116* (1), 28-32.
68. Antic, B.; Mitric, M.; Rodic, D., Structure properties and magnetic susceptibility of diluted magnetic semiconductor $Y_{2-x}Ho_xO_3$. *Journal of Magnetism and Magnetic Materials* **1995,** *145* (3), 349-356.
69. Maslen, E.; Streltsov, V.; Ishizawa, N., A synchrotron X-ray study of the electron density in *C*-type rare earth oxides. *Acta Crystallographica Section B: Structural Science* **1996,** *52* (3), 414-422.
70. Stephenson, N.; Roth, R., Structural systematics in the binary system Ta_2O_5–WO_3. V. The structure of the low-temperature form of tantalum oxide *L*-Ta_2O_5. *Acta Crystallographica Section B: Structural Crystallography and Crystal Chemistry* **1971,** *27* (5), 1037-1044.
71. Subramani, T.; Navrotsky, A., Energetics of formation and disordering in rare earth weberite RE_3TaO_7 materials. *Inorganic Chemistry* **2019,** *58* (23), 16126-16133.
72. Gussev, I. M.; O'Quinn, E. C.; Baldinozzi, G.; Neuefeind, J.; Ewing, R. C.; Zhang, F.; Lang, M., Local order of orthorhombic weberite-type Y_3TaO_7 as determined by neutron total scattering and density functional theory calculations. *Acta Materialia* **2020,** *196*, 704-709.
73. Gussev, I. M.; O'Quinn, E. C.; Tucker, M.; Ewing, R. C.; Overstreet, C.; Neuefeind, J.; Everett, M.; Zhang, Q.; Sprouster, D.; Olds, D., Systematic study of short-and long-range correlations in RE_3TaO_7 weberite-type compounds by neutron total scattering and X-ray diffraction. *Journal of Materials Chemistry A* **2023,** *11* (16), 8886-8903.
74. Kamm, G. E.; Huang, G.; Vornholt, S. M.; McAuliffe, R. D.; Veith, G. M.; Thornton, K. S.; Chapman, K. W., Relative kinetics of solid-state reactions: The role of architecture in controlling reactivity. *Journal of the American Chemical Society* **2022,** *144* (27), 11975-11979.
75. Graham, J., Crystal chemistry of complex niobium and tantalum oxides III. Relationship between *M*, *T*, and *M'* fergusonite structure. *American Mineralogist: Journal of Earth and Planetary Materials* **1974,** *59* (9-10), 1045-1046.
76. Martin, M.; Lasia, A., Influence of experimental factors on the constant phase element behavior of Pt electrodes. *Electrochimica Acta* **2011,** *56* (23), 8058-8068.
77. Irvine, J. T.; Sinclair, D. C.; West, A. R., Electroceramics: Characterization by impedance spectroscopy. *Advanced Materials* **1990,** *2* (3), 132-138.

78. Cao, Y.; Duan, N.; Yan, D.; Chi, B.; Pu, J.; Jian, L., Enhanced electrical conductivity of $LaNbO_4$ by *A*-site substitution. *International Journal of Hydrogen Energy* **2016,** *41* (45), 20633-20639.
79. Cao, Y.; Tan, Y.; Yan, D.; Chi, B.; Pu, J.; Jian, L., Electrical conductivity of Zn-doped high temperature proton conductor $LaNbO_4$. *Solid State Ionics* **2015,** *278*, 152-156.
80. Mokkelbost, T.; Kaus, I.; Haugsrud, R.; Norby, T.; Grande, T.; Einarsrud, M. A., High-temperature proton-conducting lanthanum ortho-niobate-based materials. Part II: Sintering properties and solubility of alkaline earth oxides. *Journal of the American Ceramic Society* **2008,** *91* (3), 879-886.
81. Shan, Y. J.; Kawaguchi, R.; Akizawa, R.; Tezuka, K., Crystal structure and ionic conductivity of novel rare-earth niobates *Ln*NbO_4 (*Ln* = Nd, Sm, Eu, Gd) by substituting Nb with W. *Ionics* **2023**, 1-7.
82. Norby, T.; Kofstad, P., Proton and native-ion conductivities in Y_2O_3 at high temperatures. *Solid State Ionics* **1986,** *20* (3), 169-184.
83. Bowen, M. S.; Cann, D. P.; Woodside, C., Application of the van der Pauw method for electrical conductivity measurements at high temperatures using an insulating compressing ring. *Rev. Sci. Instrum.* **2023,** *94* (11).
84. Peters, A.; Korte, C.; Hesse, D.; Zakharov, N.; Janek, J., Ionic conductivity and activation energy for oxygen ion transport in superlattices - The multilayer system CSZ (ZrO_2 + CaO)/Al_2O_3. *Solid State Ionics* **2007,** *178* (1), 67-76.
85. Fjeld, H.; Kepaptsoglou, D. M.; Haugsrud, R.; Norby, T., Charge carriers in grain boundaries of 0.5% Sr-doped $LaNbO_4$. *Solid State Ionics* **2010,** *181* (3), 104-109.
86. Haugsrud, R.; Norby, T., High-temperature proton conductivity in acceptor-substituted rare-earth ortho-tantalates, *Ln*TaO_4. *Journal of the American Ceramic Society* **2007,** *90* (4), 1116-1121.
87. Takai, S.; Kaji, S.; Yabutsuka, T.; Yao, T. In *High-Temperature Neutron Diffraction Study on $PbWO_4$ and $CaWO_4$-Based Oxide Ion Conductors with Different Defect Structure*, Electrochemical Society Meeting Abstracts 232, The Electrochemical Society, Inc.: 2017; pp 1751-1751.
88. Takai, S.; Sano, T.; Yabutsuka, T.; Yao, T. In *Difference in Oxide Ion Conduction Properties of Oxide Ion Excess and Cation Deficient $PbWO_4$ and Oxide Ion Deficient $CaWO_4$*, Electrochemical Society Meeting Abstracts 236, The Electrochemical Society, Inc.: 2019; pp 1854-1854.
89. Hu, D.; Beauvais, M. L.; Kamm, G. E.; Mullens, B. G.; Sanchez Monserrate, B. A.; Vornholt, S. M.; Chupas, P. J.; Chapman, K. W., Resolving fast relative kinetics in inorganic solid-state synthesis. *Journal of the American Chemical Society* **2023,** *145* (49), 26545-26549.

Supporting Information

Variable Temperature *In Situ* Neutron Powder Diffraction and Conductivity Studies of Undoped $HoNbO_4$ and $HoTaO_4$

Bryce G. Mullens,[1] Matilde Saura-Múzquiz,[1,2] Giulio Cordaro,[3] Frederick P. Marlton,[1,4] Helen E. Maynard-Casely,[5] Zhaoming Zhang,[5] Gianguido Baldinozzi,[3] and Brendan J. Kennedy[1,*]

[1] School of Chemistry, The University of Sydney, Sydney, New South Wales 2006, Australia

[2] Department of Materials Physics, Faculty of Physics, Universidad Complutense de Madrid, 28040, Madrid, Spain

[3] Université Paris-Saclay, Centralesupélec, Centre National de la Recherche Scientifique (CNRS), Structures, Property and Modeling of Solids (SPMS) Laboratory, 91190 Gif-sur-Yvette, France

[4] Centre for Clean Energy Technology, School of Mathematical and Physical Sciences, Faculty of Science, University of Technology Sydney, Sydney, New South Wales 2007, Australia

[5] Australian Nuclear Science and Technology Organisation, Lucas Heights, New South Wales 2234, Australia

[*] Corresponding Author: Brendan J. Kennedy (brendan.kennedy@sydney.edu.au)

Furnace Program using Wombat:

In Situ Neutron Diffraction Measurements of $HoNbO_4$:

	Temperature Range (° C)	Heating Rate (° hr^{-1})	Approx. Time (hr)
Heating	50 – 400	180	2
	400 – 1000	60	10
	1000 °C Hold	--	1
Cooling	1000 – 400	60	10
	400 – 100	180	2
		Total Time	~ 25 hours

In Situ Neutron Diffraction Measurements of $HoTaO_4$ (P2/c):

	Temperature Range (° C)	Heating Rate (° hr^{-1})	Approx. Time (hr)
Heating	100 – 1200	180	6
	1200 – 1500	60	5
	1500 °C Hold	--	1
Cooling	1500 – 1200	60	5
	1200 – 100	360	3
		Total Time	~ 20 hours

In Situ Neutron Diffraction Measurements of Ho_2O_3 + Ta_2O_5 Green Powder:

	Temperature Range (° C)	Heating Rate (° hr^{-1})	Approx. Time (hr)
Heating	100 – 1200	180	6
	1200 – 1500	30	10
	1500 °C Hold	--	4
Cooling	1500 – 1200	60	5
	1200 – 100	360	3
		Total Time	~ 28 hours

Thermogravimetric Analysis and Differential Scanning Calorimetry Analysis

Combined thermogravimetric analysis (TGA) and differential scanning calorimetry (DSC) measurements were performed using a Netzsch STA 449F3. Approximately 15 mg of $HoNbO_4$ and $HoTaO_4$ samples were weighed onto a platinum/rhodium pan with an Al_2O_3 liner and heated from room temperature to 1000 °C at a rate of 10 °C min^{-1} in air (80% N_2, 20% O_2. 20 mL min^{-1}) before being cooled to 350 °C. The measurement was then repeated after switching to an argon environment (20 mL min^{-1}).

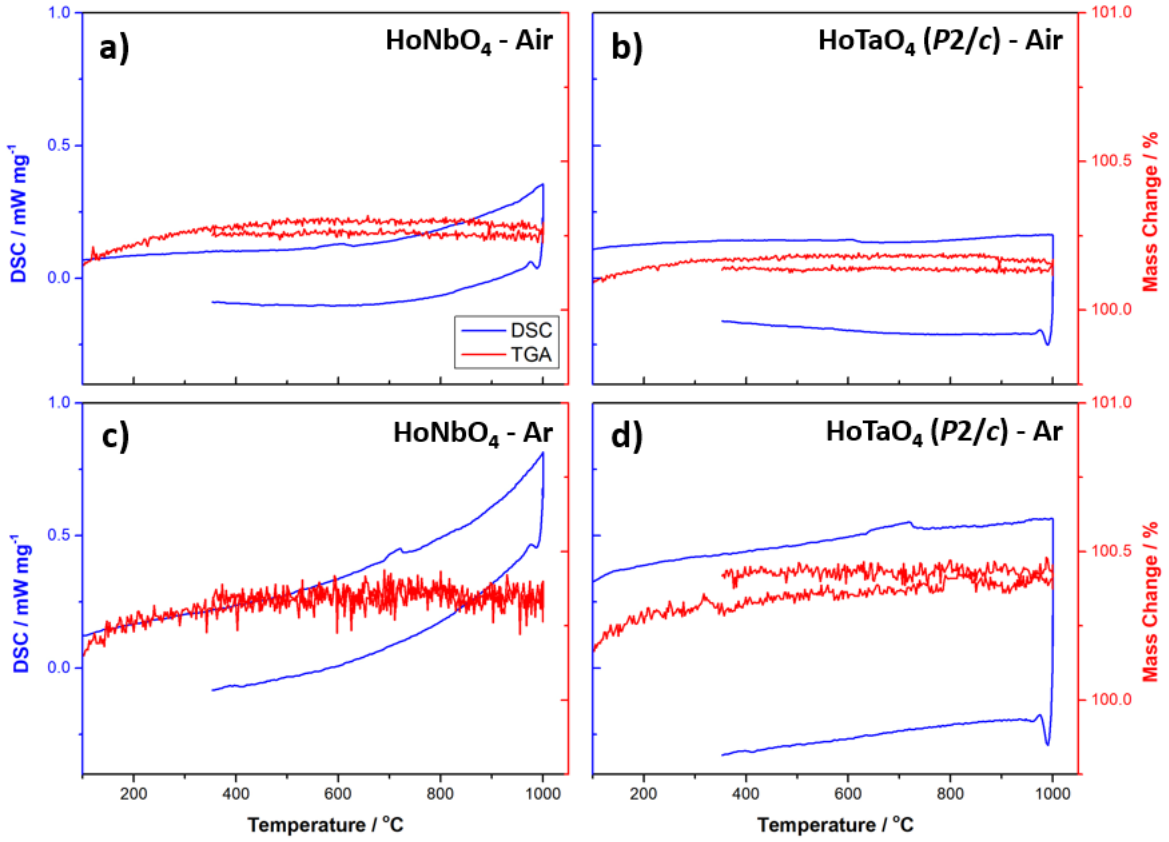

Figure S1: Thermogravimetric analysis (TGA) and differential scanning calorimetry (DSC) for (a,c) $HoNbO_4$ and (b,d) $HoTaO_4$ (*P*2/*c*). The blue line represents the DSC, whereas the red line represents the TGA. For (a,b), each sample was measured in air (80% N_2 and 20% O_2), whereas for (c,d) each sample was measured in argon. The small bumps at around 500-700 °C are below the observed *I*2/*a* to $I4_1/a$ phase transition and are suspected to be instrumental artifacts. The high temperature peak in the DSC is an artifact related to the gas change.

X-ray Fluorescence Analysis

Table S1: Cation ratios of Ho:Nb, derived using X-ray fluorescence (XRF) analysis. The sample is the measured $HoNbO_4$ sample, the standard was a 1:1 molar ratio of Ho_2O_3:Nb_2O_5 mix, and the expected is from the calculated molar ratio.

	Sample (%)	**Standard (%)**	**Expected (%)**
Ho_2O_3	61.4	55.7	58.7
Nb_2O_5	37.1	42.9	41.3

Table S2: Cation ratios of Ho:Ta, derived using X-ray fluorescence (XRF) analysis. The sample is the measured $HoTaO_4$ sample, the standard was a 1:1 molar ratio of Ho_2O_3:Ta_2O_5 mix, and the expected is from the calculated molar ratio.

	Sample (%)	**Standard (%)**	**Expected (%)**
Ho_2O_3	47.5	48.7	46.1
Ta_2O_5	52.0	50.9	53.9

Table S3: Cation ratios of Ho:Ta, derived using X-ray fluorescence (XRF) analysis. The sample is the measured Ho_2O_3 + Ta_2O_5 green powder sample, the standard was a 1:1 molar ratio of Ho_2O_3:Ta_2O_5 mix, and the expected is from the calculated molar ratio.

	Sample (%)	**Standard (%)**	**Expected (%)**
Ho_2O_3	46.3	48.7	46.1
Ta_2O_5	53.2	50.9	53.9

Table S4: Relative densities of the pallets and Calculated activation energies of the $HoNbO_4$ and $HoTaO_4$ materials from the Arrhenius plots of the electrochemical impedance spectroscopy data.

$E_{act.}$ **(eV)**	**$HoNbO_4$ ($I2/a$)**	**$HoNbO_4$ ($I4_1/a$)**	**$HoTaO_4$ ($I2/a$)**	**$HoTaO_4$ ($P2/c$)**
Wet 5% H_2 in Ar	0.82		0.74	0.78
Ar	1.08	1.58	0.97	1.01
Wet Ar	0.91	1.23	0.77	0.86
Air	1.22	1.42	1.25	1.09
Relative Density (%)	78		71	65

(i) *In Situ Neutron Diffraction Measurements of $HoNbO_4$: Observation of the Reversible $I2/a$ to $I4_1/a$ Phase Transition*

Table S5: Refined parameters for $HoNbO_4$ at low and high temperatures.

	$HoNbO_4$ (50 °C)	**$HoNbO_4$ (1000 °C)**
Space Group	$I2/a$ (#15)	$I4_1/a$ (#88)
***a* (Å)**	5.3074(3)	5.2339(2)
***b* (Å)**	10.9756(8)	= *a*
***c* (Å)**	5.0813(3)	11.1193(9)
***β* (°)**	94.444(6)	= 90
Volume (Å^3)	295.11(3)	304.60(4)
Ho *y*	0.6202(3)	= 3/8
Nb *y*	0.1430(3)	= 1/8
Ho-O (Å)	2.307(4)	2.354(3)
Ho-O (Å)	2.338(4)	--
Ho-O (Å)	2.367(5)	2.393(3)
Ho-O (Å)	2.420(4)	--
HoO_8 Vol. (Å^3)	22.75	23.47
Nb-O(1) (Å)	1.847(4)	1.888(3)
Nb-O(2) (Å)	1.930(4)	--
Nb-O(2') (Å)	2.437(4)	2.803(3)
BVS NbO_4	4.29	4.25
BVS NbO_6	4.77	4.61

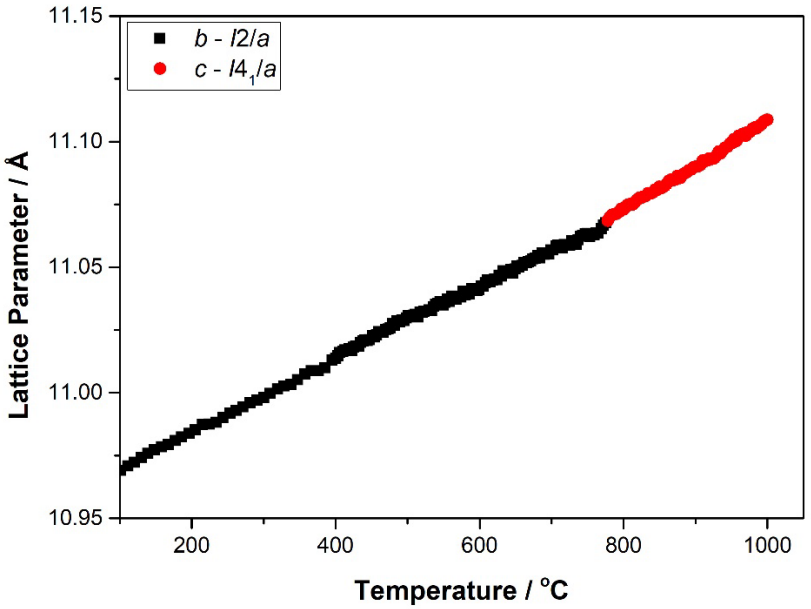

Figure S2: Temperature dependence of the lattice parameters *b* and *c* for $HoNbO_4$ obtained by Rietveld refinements against neutron powder diffraction data. The data were collected as the sample was heated from room temperature to 1000 °C, with a phase transition from $I2/a$ to $I4_1/a$ observed at ~775 °C. The error bars are smaller than the symbols.

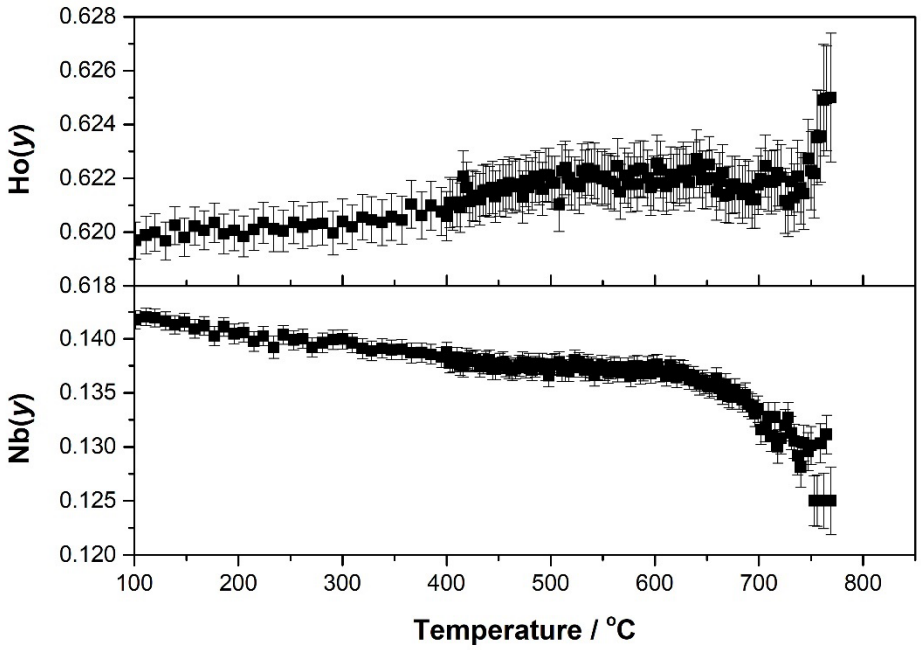

Figure S3: Temperature dependence of the Ho and Nb y atomic position parameter. As $HoNbO_4$ transforms from $I2/a$ to $I4_1/a$, the y atomic position parameters approach the special symmetric positions of 5/8 (0.625) and 1/8 (0.125) respectively.

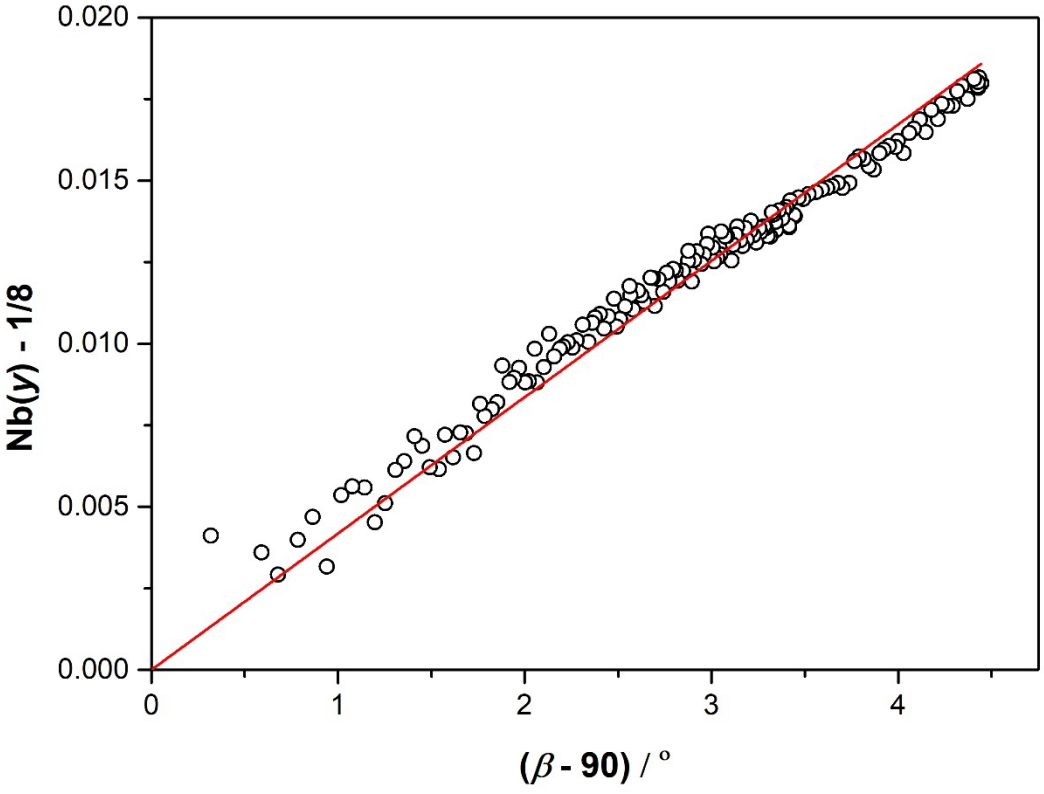

Figure S4: Temperature dependence of the Nb(y) atomic coordinate and the monoclinic β angle in $HoNbO_4$ obtained from Rietveld refinements against the NPD data.

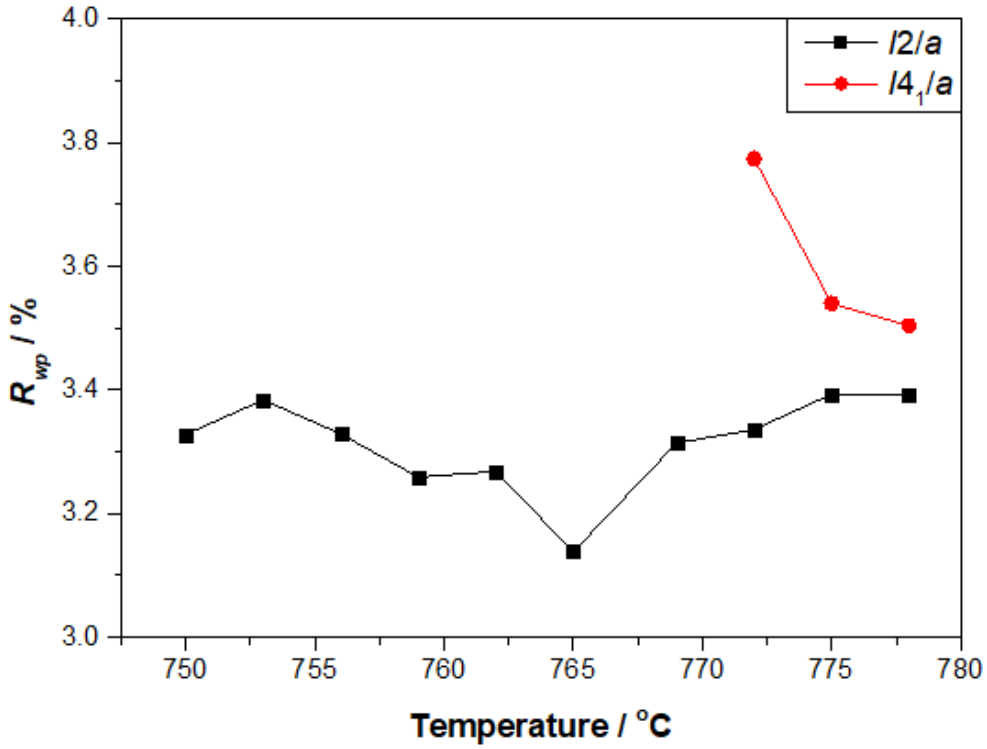

Figure S5: Plotted R_{wp} values from the variable temperature refinement of $HoNbO_4$. The region of 750-778 °C was taken as the area of interest, with T_c = 768 °C. Systematic variance across the refinements in *I*2/*a* imply that no two-phase region is necessary to fit the diffraction data across the phase transition.

Technical Details on the *I*2/*a* to *I*4$_1$/*a* Phase Transition Order Parameter

The mechanical representation of the $HoNbO_4$ tetragonal scheelite *I*4$_1$/*a* structure ($\Gamma_m, \boldsymbol{k} = 0$) decomposed to the *irrep*s of the group is

$$\Gamma_m = \begin{cases} Ho: & 2B_g \oplus 2E_g \oplus 2A_u \oplus 2E_u \\ Nb: & \oplus 2B_g \oplus 2E_g \oplus 2A_u \oplus 2E_u \\ O: & \oplus 6A_g \oplus 6B_g \oplus 3E_g \oplus 6A_u \oplus 6B_u \oplus 3E_g \end{cases}$$

which demonstrates that all atoms of the are displaced by the B_g phonons. The atomic displacements associated with the B_g soft optic mode are summarized in Table S2.

Table S6: Atomic displacements allowed by the B_g phonon in space group *I*2/*a* of the low temperature $HoNbO_4$ structure.

	δ*x*	**δ*y***	**δ*z***
Ho	0	a_1	0
Nb	0	b_2	0
O(1)	c_1	e_1	d_1
O(2)	d_2	e_2	c_2

Each of these displacements should behave according to mean-field Landau theory, at least in a temperature range close to, but below, the phase transition.

The Gibbs free energy difference expansion is corrected to account for interactions between the soft optic mode and the strain modes, which belong to either the B_g or A_g irreducible representations. The symmetry adapted strain components are $(\epsilon_1 + \epsilon_2 + \epsilon_3)$ (corresponding to volume expansion) for A_g-type strains, as well as $(\epsilon_1 - \epsilon_2)$ and ϵ_6 for the B_g-type strains. These components have the following expressions

$$(\epsilon_1 - \epsilon_2) = \frac{2(a_m - c_m)}{a_0 + c_0}$$

$$\epsilon_6 = \frac{cos\,\beta_m\,(a_m + c_m)}{\sqrt{2}(a_0 + c_0)}$$

where a_m, c_m, and β_m are the lattice parameters of the low-temperature monoclinic *I*2/*a* phase, and a_0 and c_0 are the extrapolated values from the high-temperature tetragonal *I*4$_1$/*a* phase.

Fits to the following parameters are shown below:

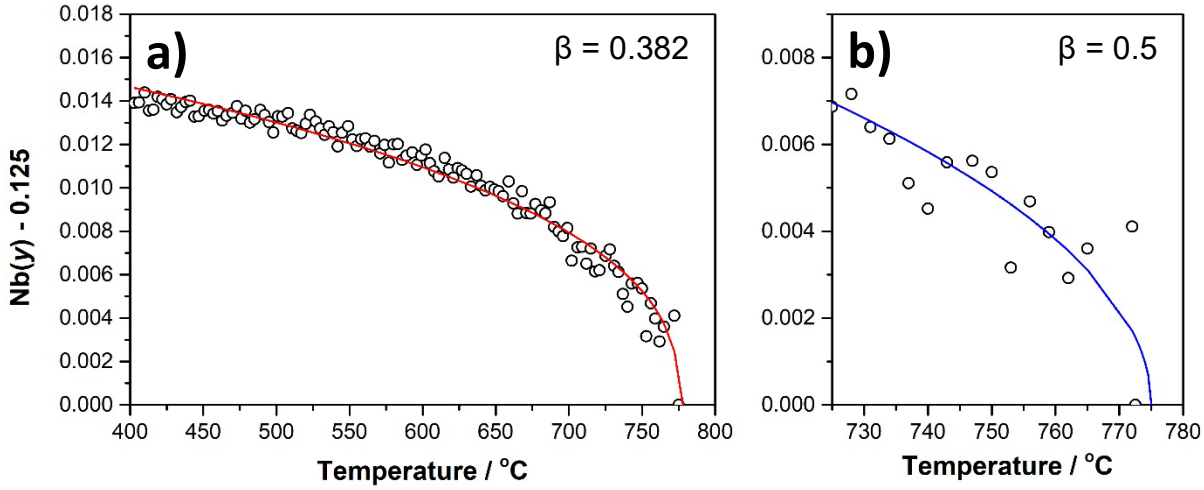

Figure S6: Atomic coordinate analysis based on the variable temperature Rietveld refinement of $HoNbO_4$, (a) fitted over the whole measured temperature range, and (b) the fit performed in a range 50 °C below T_c with the critical exponent β = 0.5. Although the data was fit down to 100 °C, the plots show from 400-800 °C for clarity.

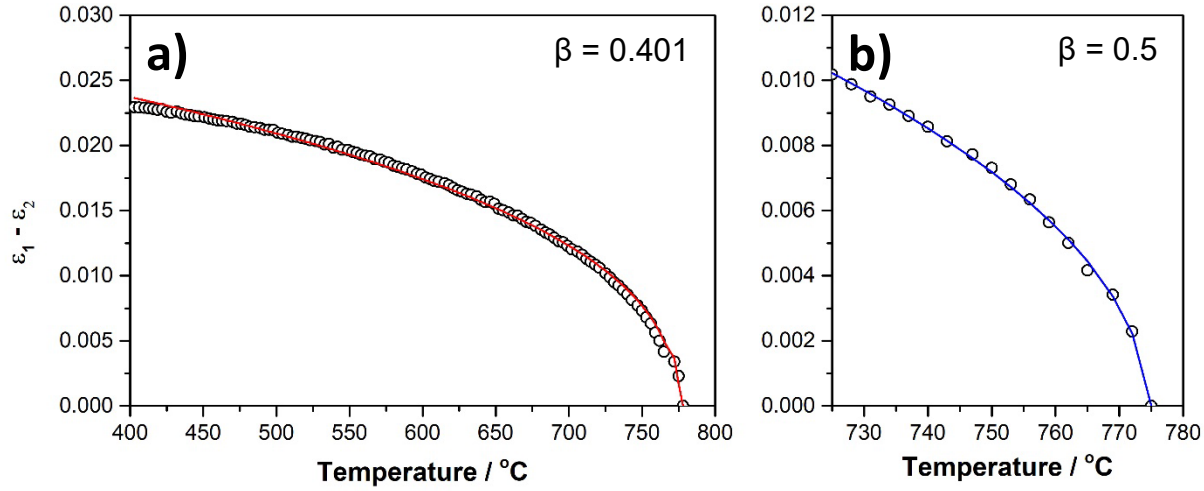

Figure S7: Strain component analysis based on the lattice parameters from the variable temperature Rietveld refinement of $HoNbO_4$, (a) fitted over the whole measured temperature range, and (b) the fit performed in a range 50 °C below T_c with the critical exponent β = 0.5. Although the data was fit down to 100 °C, the plots show from 400-800 °C for clarity.

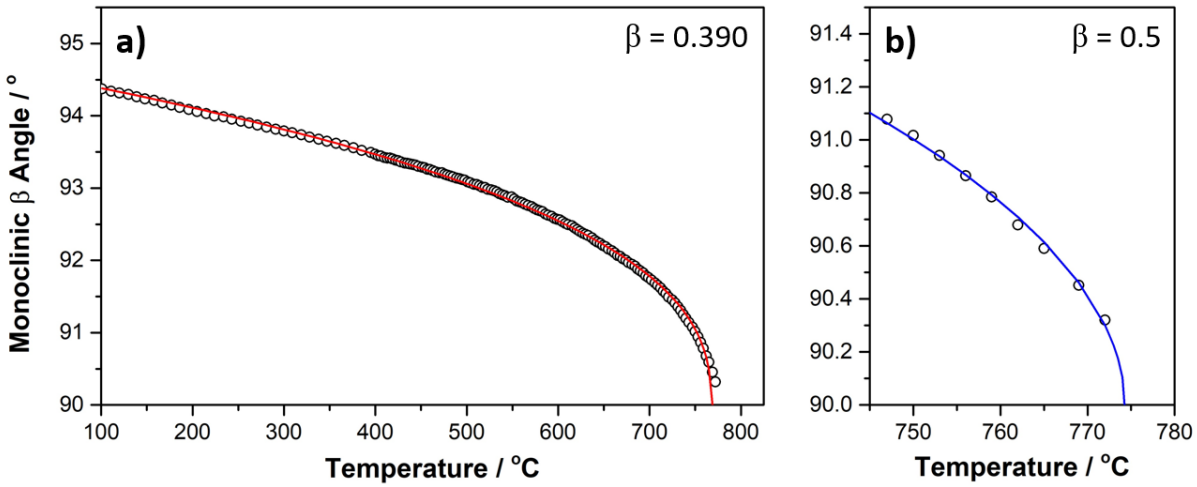

Figure S8: Monoclinic β angle analysis based on the variable temperature Rietveld refinement of $HoNbO_4$, (a) fitted over the whole measured temperature range, and (b) the fit performed in a range 50 °C below T_c with the critical exponent β = 0.5. Although the data was fit down to 100 °C, the plots show from 400-800 °C for clarity.

(ii) *In Situ Neutron Diffraction Measurements of $HoTaO_4$: Observation of the Irreversible P2/c to $I4_1/a$ Phase Transition*

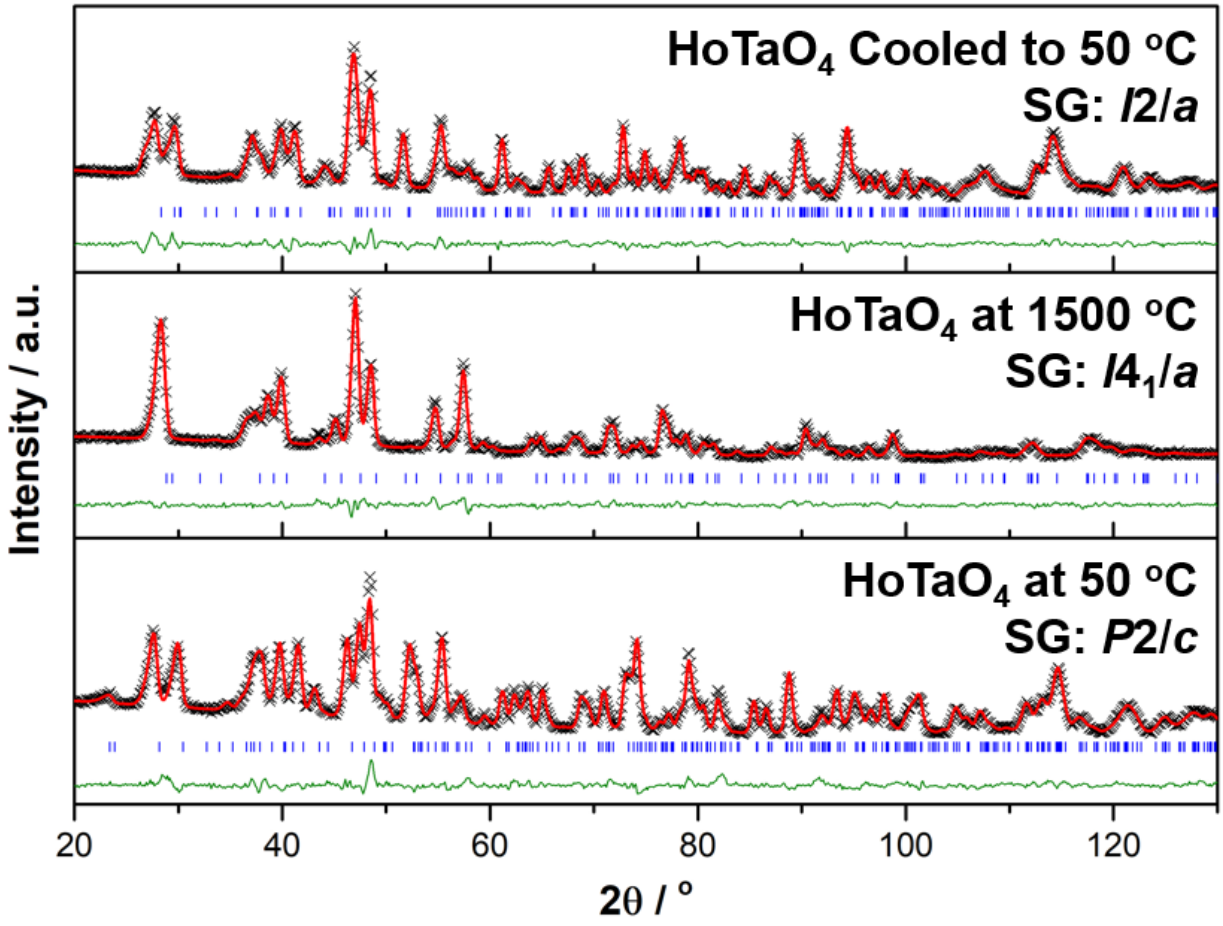

Figure S9: Rietveld refinement results for neutron powder diffraction data, measured at 1.541(1) Å. At room temperature, the structures were refined to the monoclinic *P*2/*c*, at high temperature the tetragonal $I4_1/a$, and upon cooling to 50 °C the monoclinic *I*2/*a* space groups. In all cases, the black crosses represent the observed data, the solid red line represents the fit to the measured profile, and the lower blue line represents the difference between the observed and calculated profiles. The vertical tick marks show the positions of the space group allowed Bragg reflections.

Table S7: Refined parameters for $HoTaO_4$ at low and high temperatures.

	$HoTaO_4$ (50 °C)	**$HoTaO_4$ (1500 °C)**	**$HoTaO_4$ (50 °C)**
Space Group	*P*2/*c* (#13)	$I4_1/a$ (#88)	*I*2/*a* (#15)
***a* (Å)**	5.1444(4)	5.2803(3)	5.3660(5)
***b* (Å)**	5.4926(5)	= *b*	11.0257(12)
***c* (Å)**	5.3343(4)	11.2061(10)	5.0948(5)
***β* (°)**	96.407(6)	= 90	95.320(9)
Volume ($Å^3$)	149.79(2)	312.45(4)	300.13(5)
Ho *y*	0.2333(7)	= 1/8	0.6198(5)
Nb *y*	0.3043(7)	= 1/8	0.1472(5)
Ho-O (Å)	2.304(5)	2.366(3)	2.336(6)
Ho-O (Å)	2.311(5)	--	2.340(7)
Ho-O (Å)	2.357(5)	2.412(3)	2.404(7)
Ho-O (Å)	2.554(5)	--	2.472(7)
HoO_8 Vol. ($Å^3$)	23.05	23.86	23.48
Ta-O(1) (Å)	1.882(5)	1.918(4)	1.845(7)
Ta-O(2) (Å)	2.015(5)	--	1.955(7)
Ta-O(2') (Å)	2.222(5)	2.809(3)	2.362(7)
BVS TaO_4	3.80	4.72	4.27
BVS TaO_6	4.72	--	4.88

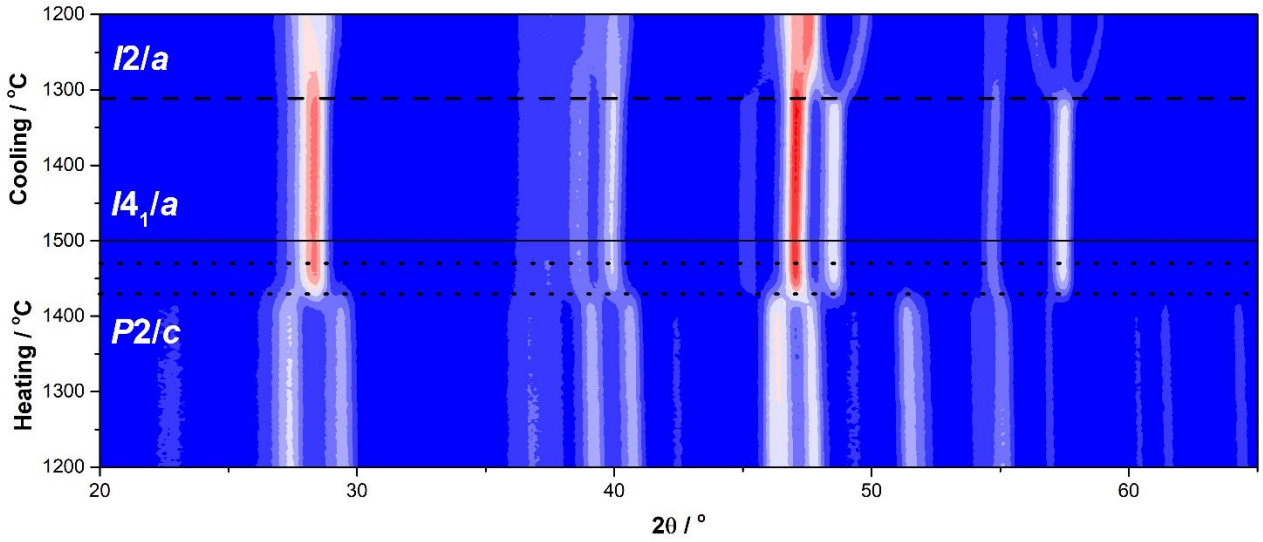

Figure S10: Portions of the temperature dependent neutron powder diffraction patterns for $HoTaO_4$ measured on heating from 1200 °C to 1500 °C and then re-cooling to 1200 °C. The *P*2/*c* and *I*4$_1$/*a* two-phase region observed upon heating is indicated by two dotted lines, and the *I*4$_1$/*a* to *I*2/*a* phase transition observed upon cooling is indicated by a dashed line. The data were collected at 1.541(1) Å.

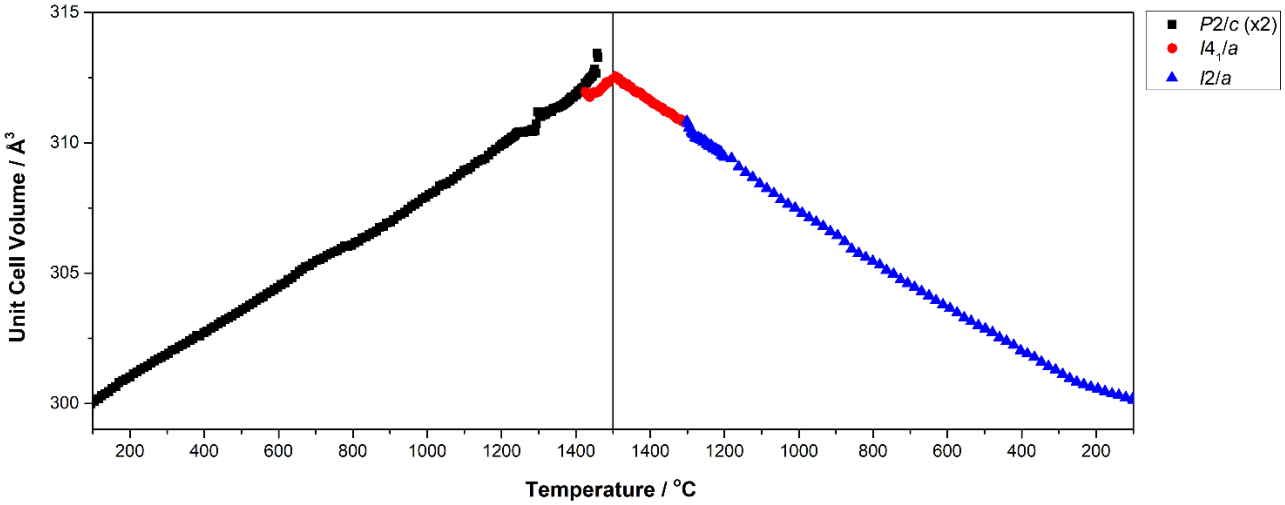

Figure S11: Temperature dependence of the unit cell volume for $HoTaO_4$ obtained by Rietveld refinements against neutron powder diffraction data. Here, the unit cell volume of the *P*2/*c* phase has been doubled for comparison. The data were collected as the sample was heated from room temperature to 1500 °C, and then as the sample was re-cooled to room temperature. The error bars are smaller than the symbols.

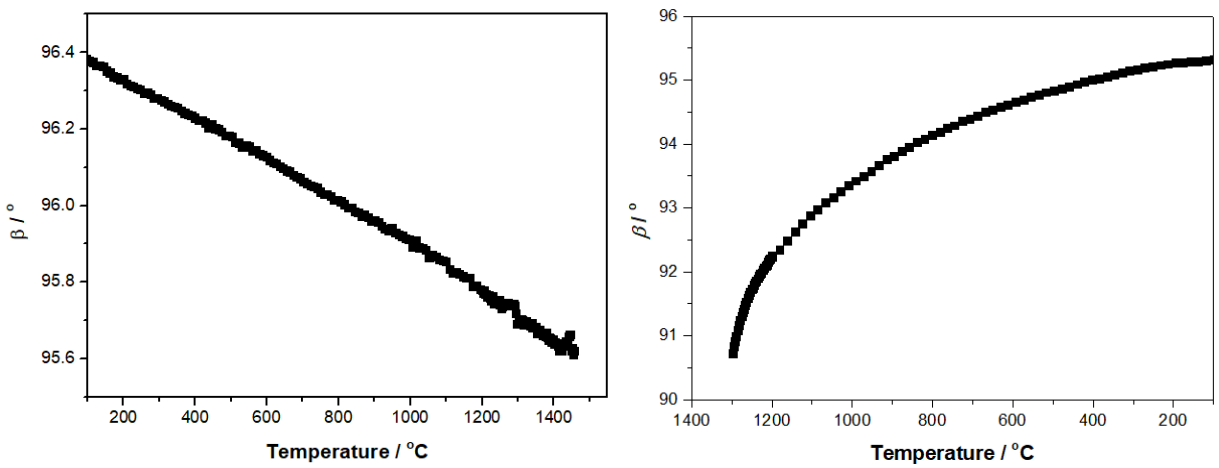

Figure S12: Beta angle (β) of the monoclinic $P2/c$ phase upon heating, and the monoclinic $I2/a$ phase upon cooling.

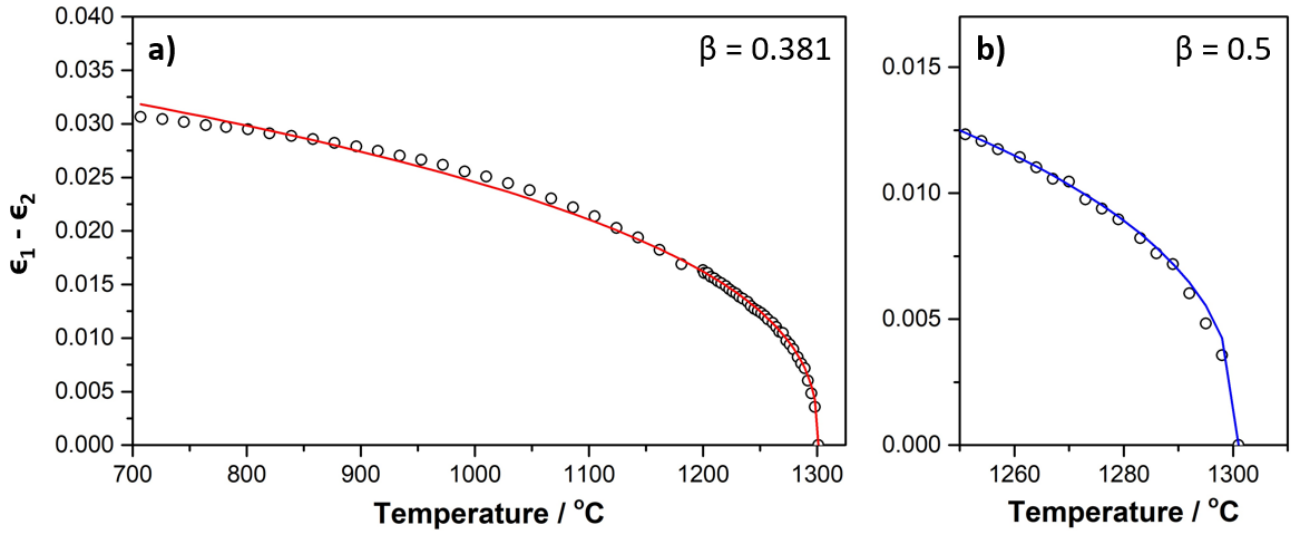

Figure S13: Strain component ($\epsilon_1 - \epsilon_2$) analysis based on the lattice parameters from the variable temperature Rietveld refinement of $HoTaO_4$, (a) fitted over the whole measured temperature range, and (b) the fit performed in a range 50 °C below T_c with the critical exponent $\beta = 0.5$. Although the data was fit down to 100 °C, the plots show from 700-1300 °C for clarity.

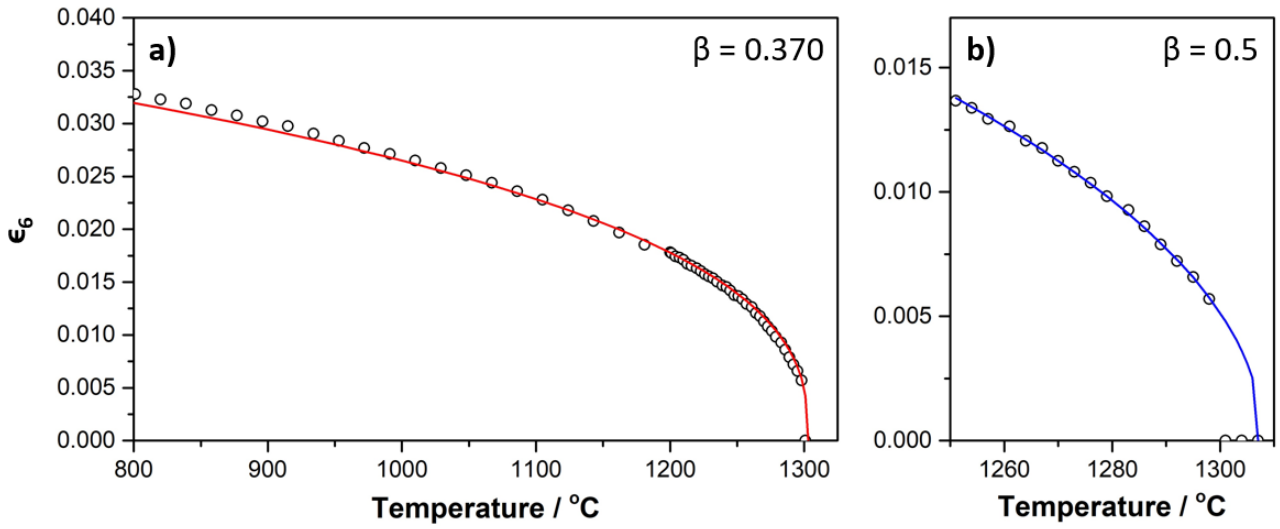

Figure S14: Strain component ϵ_6 analysis based on the lattice parameters from the variable temperature Rietveld refinement of $HoTaO_4$, (a) fitted over the 800-1300 °C temperature range, and (b) the fit performed in a range 50 °C below T_c with the critical exponent $\beta = 0.5$. Data was fit over a reduced region due to the saturation of the strain component.

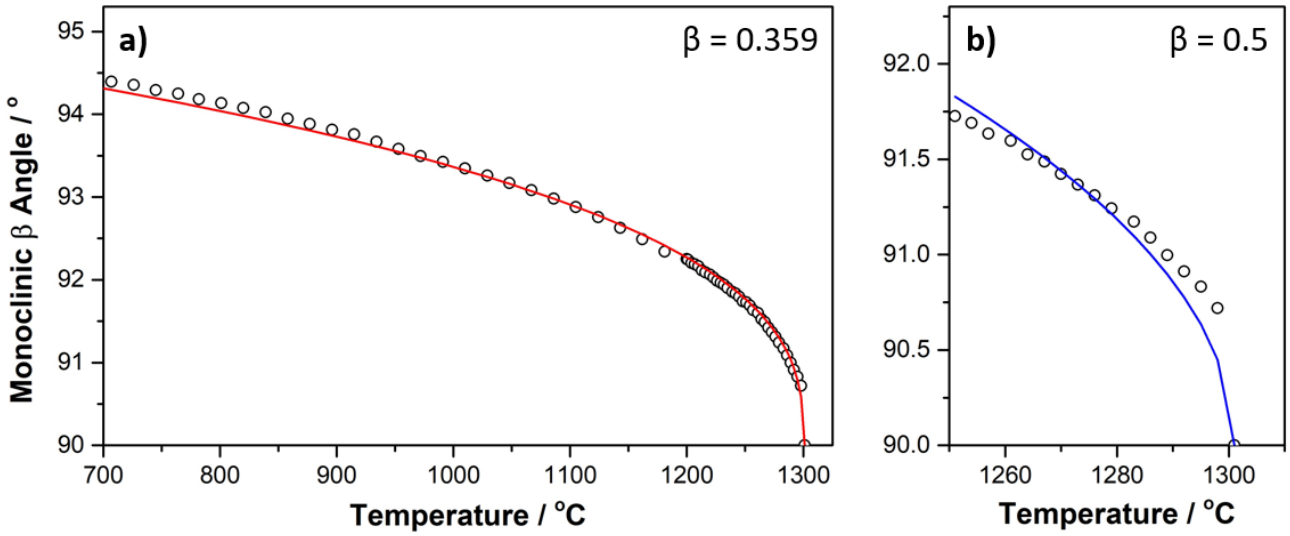

Figure S15: The monoclinic β angle analysis based on the lattice parameters from the variable temperature Rietveld refinement of $HoTaO_4$, (a) fitted over the whole measured temperature range, and (b) the fit performed in a range 50 °C below T_c with the critical exponent $\beta = 0.5$. Although the data was fit down to 100 °C, the plots show from 700-1300 °C for clarity.

(iii) *In Situ Neutron Diffraction Measurements of Ho_2O_3 + Ta_2O_5 Green Powder: Observation of an Intermediate $C222_1$ Phase*

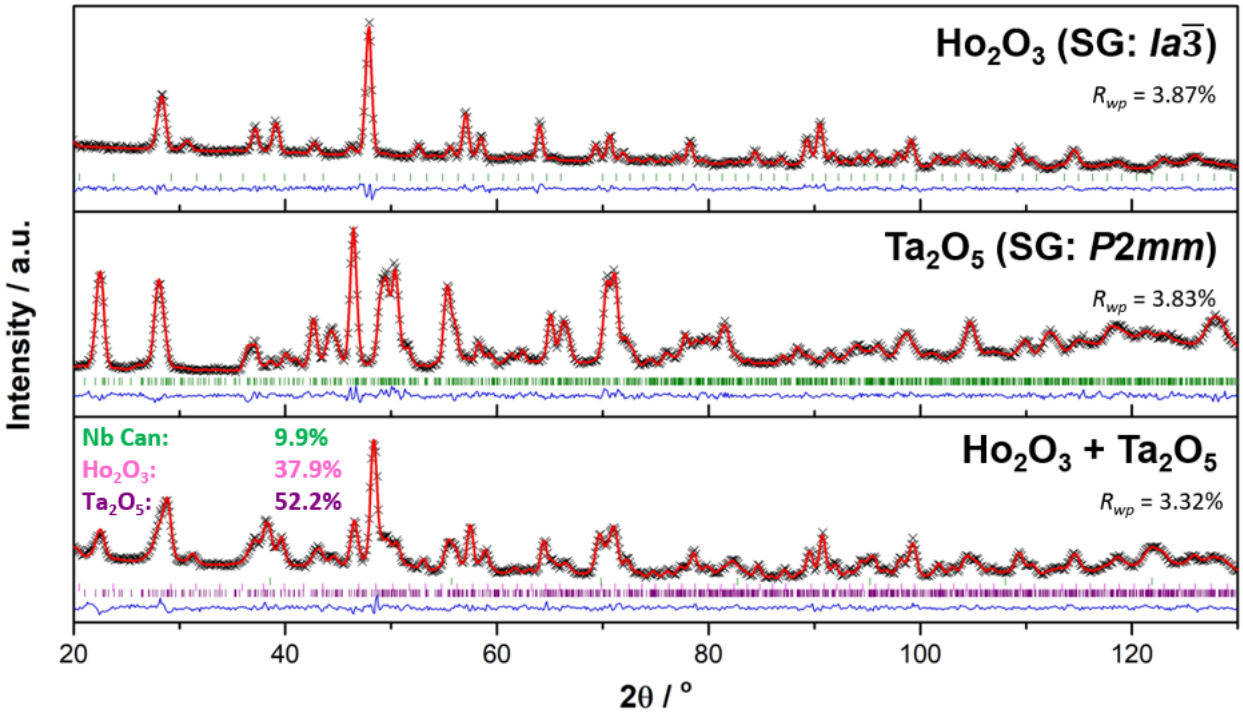

Figure S16: Rietveld refinement results for room temperature neutron powder diffraction data, measured at 1.541(1) Å. In all cases, the black crosses represent the observed data, the solid red line represents the fit to the measured profile, the lower blue line represents the difference between the observed and calculated profiles. The vertical tick marks show the positions of the space group allowed Bragg reflections.

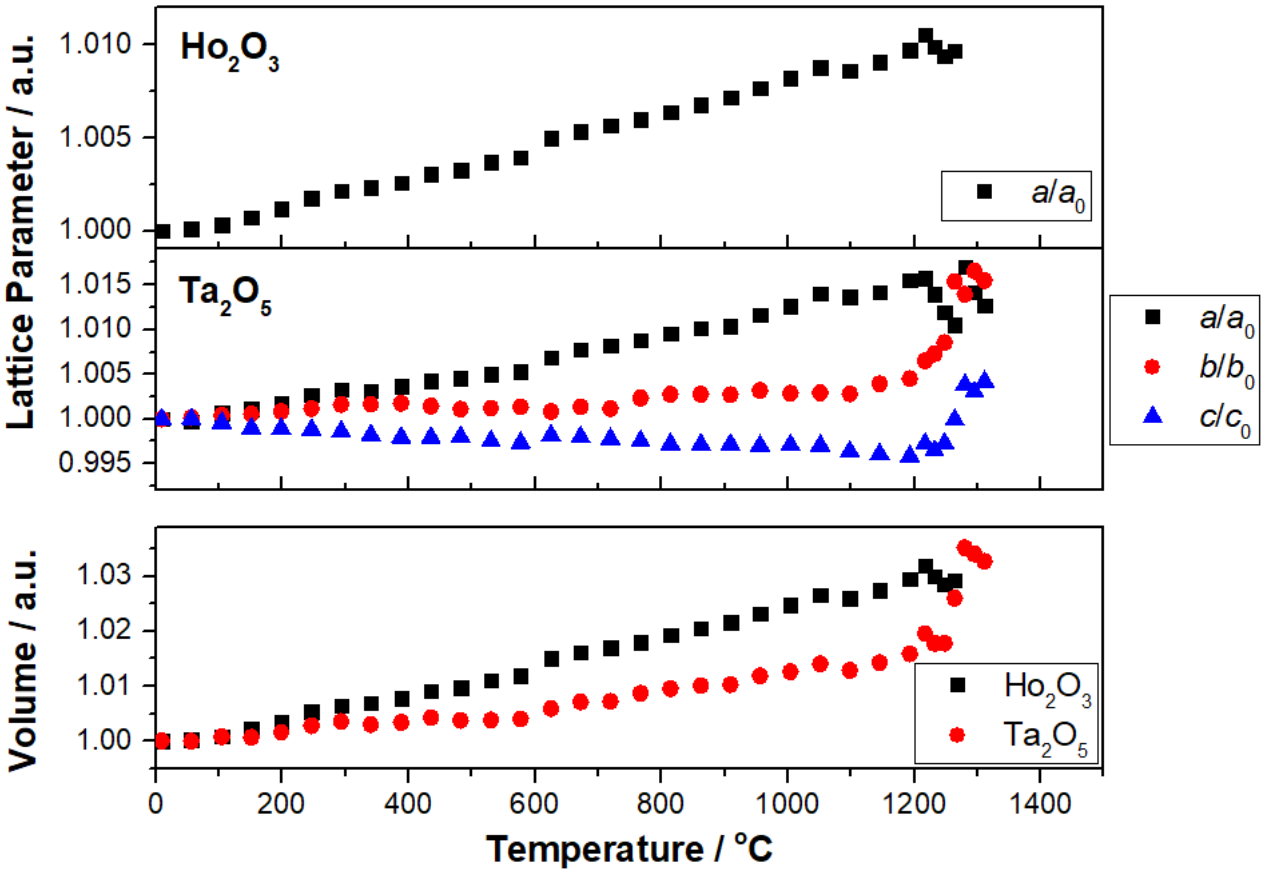

Figure S17: (Top) Normalized lattice parameters for Ho_2O_3 and Ta_2O_5 evolving with temperature. (Bottom) Normalized unit cell volume for Ho_2O_3 and Ta_2O_5, showing thermal expansion.

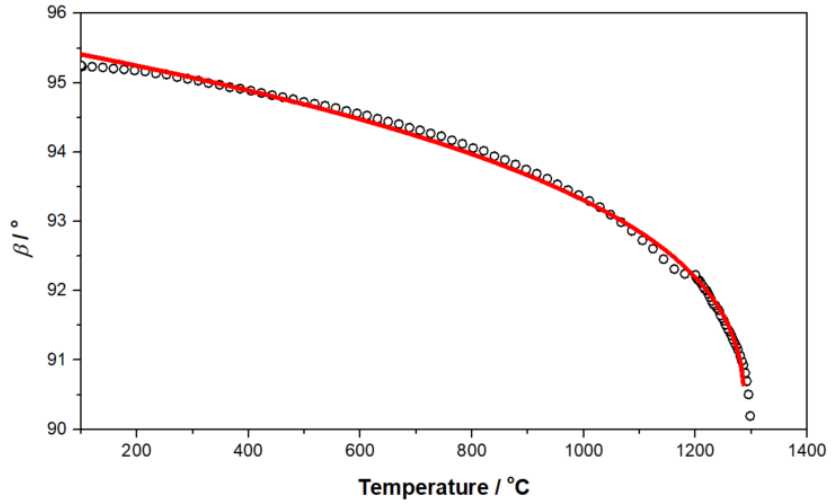

Figure S18: Temperature dependence of the monoclinic β angle of $I2/a$ against temperature for $HoTaO_4$ upon cooling. The black circles are the refined values, and the solid red line is the fit to the expression $f(T) = A(T_C - T)^{\eta}$, where A is a general prefactor, T is the observed temperature, T_c is the transition temperature, and η is a fitting exponent.

(iv) *Ionic Conductivity Studies of P2/c and I2/a Fergusonite-Type Structures*

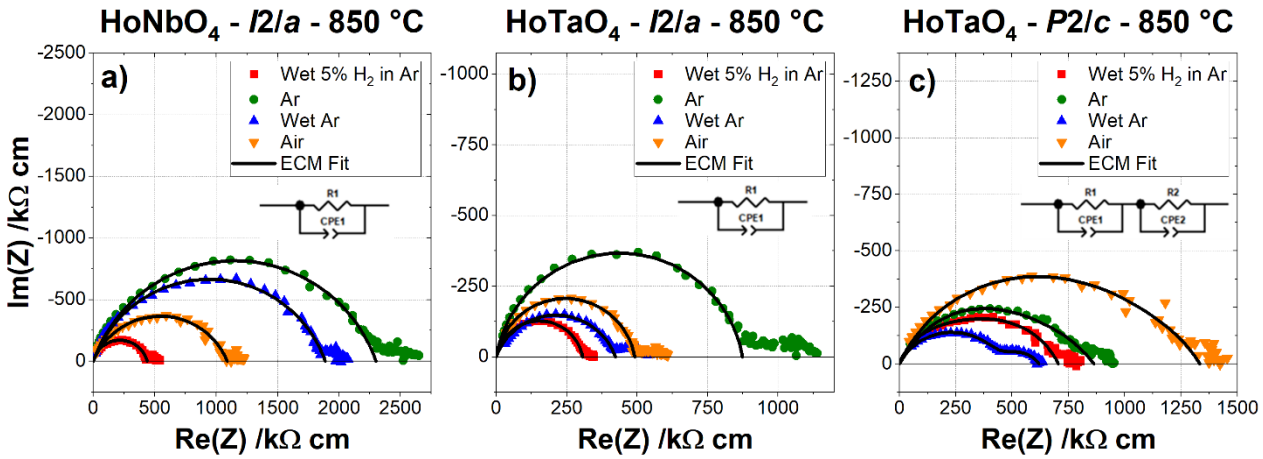

Figure S19: Impedance results in Nyquist plots for $HoNbO_4$ - *I2/a* (a), $HoNbO_4$ - *I2/a* (b), and $HoNbO_4$ - *P2/c* (c) for different atmospheres at 850 °C. The ECM fittings and the circuit used for the simulations are also reported.

Table S1: Bond distances derived from the Rietveld refinements to the NPD data of $HoNbO_4$ and $HoTaO_4$.

	$HoNbO_4$ (*I2/a*)	**$HoNbO_4$ (*I4₁/a*)**	**$HoTaO_4$ (*I2/a*)**	**$HoTaO_4$ (*P2/c*)**
O(1)-O(1) (Å)	2.798(3)	2.738(2)	2.826(4)	2.814(3)
O(1)-O(1) (Å)	2.921(7)	2.875(7)	2.871(11)	3.005(8)
O(1)-O(2) (Å)	2.891(5)	2.835(7)	2.900(8)	2.895(6)
Average (Å)	2.87(4)	2.82(4)	2.87(2)	2.93(6)
***B-B* (Å)**	4.110(6)	3.818(2)	4.211(9)	4.276(7)

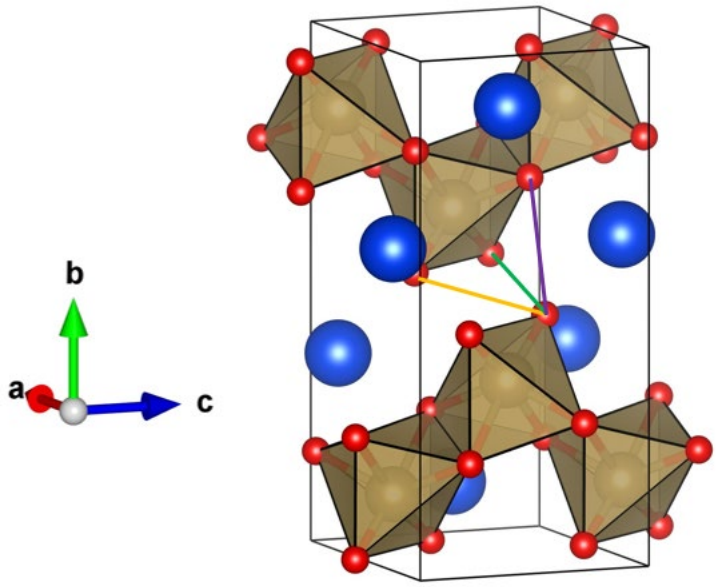

Figure S20: Refined structure of $HoTaO_4$ (*I*2/*a*) at room temperature. The green and orange lines represent the O(1)-O(1) distances, whilst the purple line represents the O(1)-O(2) distance.

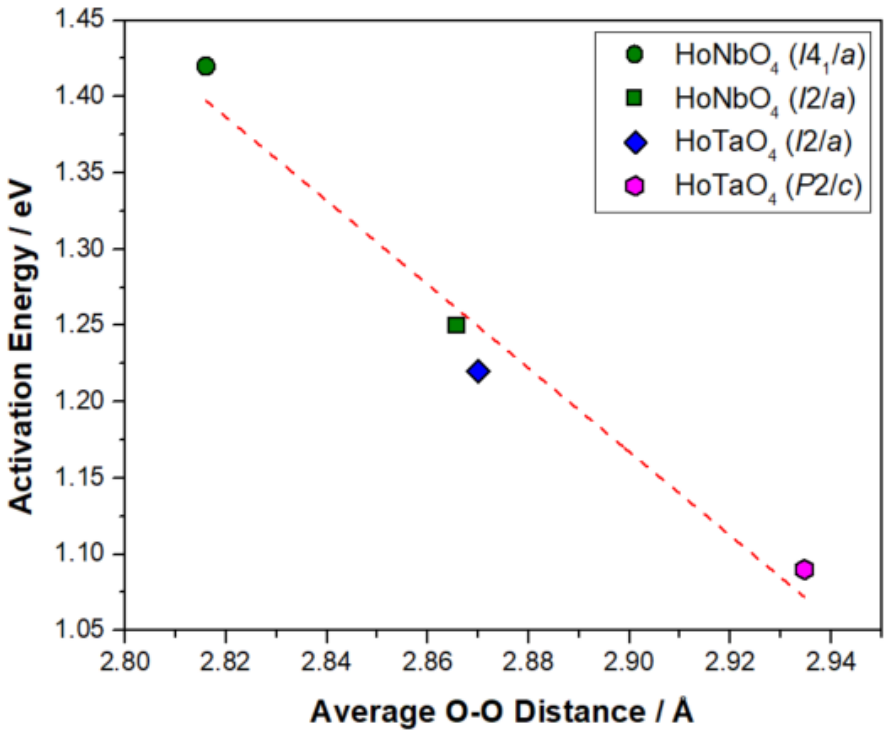

Figure S21: Relationship between the activation energy calculated from the air electrochemical impedance spectroscopy and the average O-O distances taken from the Rietveld refinements to the NPD datasets.